Computers and Mathematics with Applications 147 (2023) 92–110

Contents lists available at ScienceDirect

Computers and Mathematics with Applications

journal homepage: www.elsevier.com/locate/camwa

Semi and fully discrete error analysis for elastodynamic interface problems using immersed finite element methods

Yuan Chen [a], Songming Hou [b], Xu Zhang [c,*]

[a] Department of Mathematics, The Ohio State University, Columbus, OH 43210, USA
[b] Program of Mathematics & Statistics and Center of Applied Physics, Louisiana Tech University, Ruston, LA 71272, USA
[c] Department of Mathematics, Oklahoma State University, Stillwater, OK 74078, USA

ARTICLE INFO

Keywords:
Elastodynamics
Interface problem
Immersed finite element

ABSTRACT

In this paper, we present an immersed finite element (IFE) method for solving the elastodynamics interface problems on interface-unfitted meshes. For spatial discretization, we use vector-valued $\mathcal{P}_1$ and $\mathcal{Q}_1$ IFE spaces. We establish some important properties of these IFE spaces, such as inverse inequalities, which will be crucial in the error analysis. For temporal discretization, both the semi-discrete and the fully discrete schemes are derived. The proposed schemes are proved to be unconditionally stable and enjoy optimal rates of convergence in the energy, L^2 and semi-H^1 norms. Numerical examples are designed to verify our theoretical analysis and to demonstrate the stability and robustness of our schemes.

1. Introduction

In this paper, we consider the following two-dimensional elastodynamics interface problem:

$$\mathbf{u}_{tt} - \operatorname{div}\sigma(\mathbf{u}) = \mathbf{f}, \qquad \text{in } \Omega^- \cup \Omega^+, t \in [0, L], \tag{1.1a}$$

$$\mathbf{u}(\mathbf{x}, 0) = \boldsymbol{\omega}_0(\mathbf{x}), \qquad \text{in } \Omega^- \cup \Omega^+, \tag{1.1b}$$

$$\mathbf{u}_t(\mathbf{x}, 0) = \boldsymbol{\omega}_1(\mathbf{x}), \qquad \text{in } \Omega^- \cup \Omega^+, \tag{1.1c}$$

$$\mathbf{u} = \mathbf{g}(\mathbf{x}, t), \qquad \text{on } \partial\Omega, t \in [0, L]. \tag{1.1d}$$

Here, $\Omega \subset \mathbb{R}^2$ is assumed to be a polygonal domain separated by a fixed interface Γ such that $\overline{\Omega} = \overline{\Omega^+ \cup \Omega^- \cup \Gamma}$, as illustrated in Fig. 1. The unknown function $\mathbf{u} : \Omega \times [0, L] \to \mathbb{R}^2$ denotes the displacement vector field of the elastic body, and $\mathbf{f}$ is a given external body force. The stress tensor $\sigma = (\sigma_{ij}(\mathbf{u}))$, $1 \le i, j \le 2$ is defined to be

$$\sigma_{ij}(\mathbf{u}) = \lambda(\nabla \cdot \mathbf{u})\delta_{ij} + 2\mu\epsilon_{ij}(\mathbf{u}), \tag{1.1e}$$

where δ_{ij} is the Kronecker delta function and λ and μ are Lamé parameters. The linearized strain tensor $\epsilon(\mathbf{u}) = (\epsilon_{ij}(\mathbf{u}))$ is defined by

$$\epsilon_{ij}(\mathbf{u}) = \frac{1}{2}\left(\frac{\partial u_i}{\partial x_j} + \frac{\partial u_j}{\partial x_i}\right). \tag{1.1f}$$

Two subdomains Ω^+ and Ω^- are occupied by two different elastic materials with distinct Lamé parameters λ and μ. Without loss of generality, we assume that the Lamé parameters are piecewise constant defined as follows:

$$\lambda = \begin{cases} \lambda^-, & \text{if } \mathbf{x} \in \Omega^-, \\ \lambda^+, & \text{if } \mathbf{x} \in \Omega^+, \end{cases} \qquad \mu = \begin{cases} \mu^-, & \text{if } \mathbf{x} \in \Omega^-, \\ \mu^+, & \text{if } \mathbf{x} \in \Omega^+. \end{cases} \tag{1.1g}$$

In addition, we assume the following interface conditions across the interface Γ at any time $t \in [0, L]$:

* Corresponding author.
E-mail addresses: chen.11050@buckeyemail.osu.edu (Y. Chen), shou@latech.edu (S. Hou), xzhang@okstate.edu (X. Zhang).

https://doi.org/10.1016/j.camwa.2023.07.014
Received 27 January 2023; Received in revised form 19 June 2023; Accepted 15 July 2023

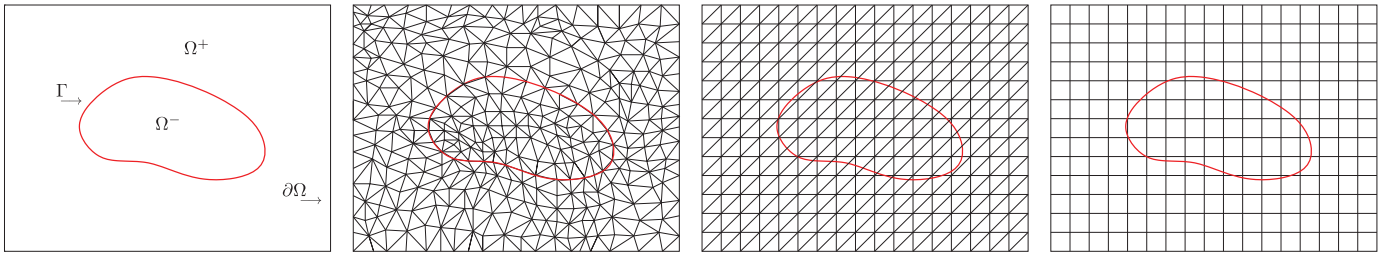

Fig. 1. From left: a domain of the elastodynamic interface problem, a fitted triangular mesh, an unfitted triangular mesh, an unfitted Cartesian mesh.

$$[\![\mathbf{u}]\!]_\Gamma = \mathbf{0}, \text{ on } \Gamma, \tag{1.1h}$$

$$[\![\sigma(\mathbf{u})\mathbf{n}]\!]_\Gamma = \mathbf{0}, \text{ on } \Gamma, \tag{1.1i}$$

where the jump operator $[\![\cdot]\!]_\Gamma$ is defined to be $[\![\mathbf{v}]\!]_\Gamma := (\mathbf{v}|_{\Omega^+})_\Gamma - (\mathbf{v}|_{\Omega^-})_\Gamma$, and $\mathbf{n}$ is the unit normal pointing from Ω^- to Ω^+.

The present work is motivated by wide applications of elastodynamics in the real-world engineering field. In the past decades, the study of elastic wave propagation is of great interest in many applications originated from seismology, evaluation of composites, ocean acoustics, and biomechanics [14,15,39,41,42]. For example, the propagation of seismic waves in the layered earth can be modeled by elastodynamics in inhomogeneous media. Another example in the biomechanical applications is the modeling of thorax by a bi-material medium consisting of thoracic wall and lung to investigate the transmission of energy through human bodies [13–15]. In these real scenarios, difficulties often occur when elastic waves propagate through medias with complicated material interface geometry, so it is desirable to design efficient and accurate simulation techniques.

Many studies have been carried out to numerically solve steady-state elasticity interface problems. Roughly speaking, there are two classes of numerical methods among the literature, named fitted-mesh and unfitted-mesh methods. For the first class, the computational mesh is generated to align with the interface (second plot of Fig. 1), so that standard discretization techniques, such as finite element method [5,50], discontinuous Galerkin method [10,23], weak Galerkin method [37,43] can be directly applied without sacrificing their accuracy. However, it is rather expensive to construct high-quality fitted meshes especially when the interface has complex geometries or the interface evolves with time. Another class of methods, known as unfitted-mesh methods, allows us to use meshes independent of interfaces without compromising its accuracy (right two plots in Fig. 1). Thus, these methods are often more efficient in computations. Existing numerical methods in this class include immersed interface method (IIM) [7,48], multi-scale finite element method [9], extended finite element method (XFEM) [11], CutFEM [24,40] and immersed finite element method (IFEM), to name only a few.

The IFEM is a class of unfitted-mesh finite element methods for solving PDE interface problems. IFEM modifies the local finite element spaces on interface elements by incorporating interface conditions to maintain optimal approximation property. Unlike other unfitted methods aforementioned, a distinctive feature of IFEM is the degree of freedom (DoF) is independent of the interface locations, since the IFE space is isomorphic to the standard FE space on the same mesh. So far, the IFEM has been developed for many PDE interface problems, including elliptic problems [19,21,26,32], Stokes problems [8,29]. For elasticity interface problems, we refer readers to [12,33,35,38,28] for the construction of immersed $\mathcal{P}_1$, $\mathcal{Q}_1$, rotated-$\mathcal{Q}_1$ and $\mathcal{P}_1/C\mathcal{R}$ finite element spaces, [17,18] for error analysis of IFEM for $\mathcal{P}_1$, $\mathcal{Q}_1$ spaces and [27] for a Petrov-Galerkin type method.

Besides the aforementioned steady-state applications, the IFEM can also be used as spatial discretization for solving time-dependent PDE interface problems. In [34] and [47], the authors developed and analyzed both semi-discrete and fully discrete IFE schemes for parabolic and hyperbolic interface problems, respectively. In [36] and [2], the error analysis for this numerical scheme has been improved by requiring less restrictive regularity of solution. Several IFE methods for time-dependent Stokes and Navier-Stokes equations with stationary and moving interfaces have been introduced in [30,44].

In this paper, we develop and analyze an IFE method for elastodynamics interface problems based on unfitted triangular or rectangular meshes. For the spatial discretization, we employ the vector-valued immersed $\mathcal{P}_1$ and $\mathcal{Q}_1$ IFE spaces introduced in [17,18]. We further prove the inverse inequalities of these IFE functions, which are essential in our error estimation. A semi-discrete IFE scheme is proposed and optimal error estimates in the energy, L^2 and semi-H^1 norm are theoretically proved. For full discretization, we adopt the θ-scheme and prove the optimal convergence rates in L^2 and semi-H^1 norm, as well as the unconditional stability. The constant in our error bounds is independent of interface location. Comparing to the immersed discontinuous Galerkin method introduced in [1] for acoustic-elastic and elastic-elastic wave propagation problem, the auxiliary variable is not required in our scheme for numerical stability. Consequently, our method is less expensive since fewer degrees of freedom are used in our method. For elastodynamic interface problems with nonhomogeneous interface jump conditions, i.e., the right hand side of (1.1h) and (1.1i) are nonzero, the IFE space can be constructed naturally following the homogenization idea in [26]. However, the approximation properties and the *a priori* error estimates require significant amount of work, hence the authors will not consider this case in the current paper.

The rest of the paper is organized as follows. In Section 2, we recall the $\mathcal{P}_1$ and $\mathcal{Q}_1$ IFE spaces for stationary elasticity interface problems. In Section 3, we introduce semi-discrete and fully discrete schemes for solving elastodynamics problems. In Section 4, we prove the inverse inequalities of the these vector-valued IFE spaces and prove the optimal convergence for the proposed semi and fully discrete numerical schemes. In Section 5, we report several numerical examples to verify the theoretical results and explore other features of the proposed schemes. Brief conclusions are summarized in Section 6.

2. IFE discretization

In this section, we first introduce some notations and assumptions to be used in this paper, then we recall the linear and bilinear immersed finite element spaces for the stationary elasticity problems. We refer [18,33] for more details of the construction and analysis.

2.1. Notations and assumptions

We denote the standard Sobolev space on a measurable set $\tilde{\Omega} \subset \Omega$ as $W^{k,p}(\tilde{\Omega})$ equipped with the norm $\|\cdot\|_{W^{k,p}(\tilde{\Omega})}$ and the semi-norm $|\cdot|_{W^{k,p}(\tilde{\Omega})}$. As usual, we write $W^{k,2}(\tilde{\Omega})$ simply as $H^k(\tilde{\Omega})$ when $p=2$. For a vector function $\mathbf{w} = (w_i)_{i=1,2} \in \mathbf{W}^{k,p}(\tilde{\Omega}) = [W^{k,p}(\tilde{\Omega})]^2$, its norm is naturally defined by

$$\|\mathbf{w}\|_{\mathbf{W}^{k,p}(\tilde{\Omega})} = \sum_{i=1}^{2} \|w_i\|_{W^{k,p}(\tilde{\Omega})}. \tag{2.1}$$

The semi-norm $|\cdot|_{\mathbf{W}^{k,p}(\tilde{\Omega})}$ is defined similarly.

In the case of $\tilde{\Omega} \cap \Gamma \neq \emptyset$, we denote the subsets $\tilde{\Omega} \cap \Omega^s$ by $\tilde{\Omega}^s$ for $s = +, -$. The broken Sobolev space defined on $\tilde{\Omega}$ is denoted by $\mathbf{PW}^{k,p}(\tilde{\Omega})$

$$\mathbf{PW}^{k,p}(\tilde{\Omega}) = \{\mathbf{v} : \mathbf{v}|_{\tilde{\Omega}^s} \in [W^{k,p}(\tilde{\Omega}^s)]^2, s = +, -; \ \ [\![\mathbf{v}]\!]_\Gamma = [\![\sigma(\mathbf{v})\mathbf{n}]\!]_\Gamma = \mathbf{0}\}. \tag{2.2}$$

The associated norm $\|\cdot\|_{\mathbf{PW}^{k,p}(\tilde{\Omega})}$ and semi-norm $|\cdot|_{\mathbf{PW}^{k,p}(\tilde{\Omega})}$ are defined by:

$$\|\mathbf{v}\|_{\mathbf{PW}^{k,p}(\tilde{\Omega})} = \sum_{s=\pm} \|\mathbf{v}\|_{[W^{k,p}(\tilde{\Omega}^s)]^2}, \quad |\mathbf{v}|_{\mathbf{PW}^{k,p}(\tilde{\Omega})} = \sum_{s=\pm} |\mathbf{v}|_{[W^{k,p}(\tilde{\Omega}^s)]^2}. \tag{2.3}$$

Similar to standard Sobolev spaces, we denote the broken Sobolev space $\mathbf{PW}^{k,2}(\tilde{\Omega})$ by $\mathbf{PH}^k(\tilde{\Omega})$ with norm $\|\cdot\|_{\mathbf{PH}^k(\tilde{\Omega})}$. The space $\mathbf{PH}^2(\tilde{\Omega})$ will be used frequently in our analysis since the exact solution is assumed to have a piecewise H^2 regularity, i.e. $\mathbf{u}(\cdot, t) \in \mathbf{PH}^2(\tilde{\Omega})$.

Furthermore, we define the time-dependent Sobolev space $L^p(0, L; \mathbf{V})$

$$L^p(0, L; \mathbf{V}) = \left\{ \mathbf{v} : [0, L] \mapsto \mathbf{V}, \int_0^L \|\mathbf{v}(\cdot, t)\|_{\mathbf{V}}^p dt < \infty \right\}, \quad p \in \mathbb{N}^+, \tag{2.4}$$

with the norm

$$\|\mathbf{v}\|_{L^p(0,L;\mathbf{V})} = \left(\int_0^L \|\mathbf{v}(\cdot, t)\|_{\mathbf{V}}^p dt \right)^{1/p}. \tag{2.5}$$

When $p = \infty$, the corresponding space is defined as

$$L^\infty(0, L; \mathbf{V}) = \left\{ \mathbf{v} : [0, L] \mapsto \mathbf{V}, \sup_{t \in [0,L]} \|\mathbf{v}(\cdot, t)\|_{\mathbf{V}} < \infty \right\}, \tag{2.6}$$

with the norm

$$\|\mathbf{v}\|_{L^\infty(0,L;\mathbf{V})} = \sup_{t \in [0,L]} \|\mathbf{v}(\cdot, t)\|_{\mathbf{V}}. \tag{2.7}$$

Similarly, $W^{k,p}(0, L; \mathbf{V})$ can be defined with associated norm:

$$\|\mathbf{v}\|_{W^{k,p}(0,L;\mathbf{V})} = \left(\sum_{|\alpha| \le k} \left\| D^\alpha \left(\|\mathbf{v}(\cdot, t)\|_{\mathbf{V}} \right) \right\|_{L^p(0,L)}^p \right)^{1/p}. \tag{2.8}$$

As usual, when $p = 2$, we simply write the space $W^{k,2}(0, L; \mathbf{V})$ as $H^k(0, L; \mathbf{V})$.

Let $\mathcal{T}_h$ be a shape-regular triangular or rectangular mesh of Ω. We use $\mathcal{N}_h$ and $\mathcal{E}_h$ to denote the set of nodes and edges, respectively. For each $T \in \mathcal{T}_h$, $h_T := \text{diam}(T)$ is the diameter of T, and the mesh size is determined by $h := \max_{T \in \mathcal{T}_h} \{h_T\}$. An element $T \in \mathcal{T}_h$ is called an interface element if $T \cap \Gamma \neq \emptyset$; otherwise, it is called a non-interface element. The collections of interface elements and noninterface elements are denoted as $\mathcal{T}_h^i$ and $\mathcal{T}_h^n$, respectively. For an interface element T, we use $T^+ = T \cap \Omega^+$ and $T^- = T \cap \Omega^-$ to denote its two subelements. The collection of edges intersecting with the interface Γ is denoted as $\mathcal{E}_h^i$, and $\mathcal{E}_h^n = \mathcal{E}_h \backslash \mathcal{E}_h^i$ denotes the set of the non-interface edges. The sets of interior and boundary edges are denoted by $\mathring{\mathcal{E}}_h$ and $\mathcal{E}_h^b$, respectively. Similarly, $\mathring{\mathcal{E}}_h^i$ and $\mathring{\mathcal{E}}_h^n$ denote the sets of interior interface edges and interior non-interface edges, respectively.

For every interior edge $e \in \mathring{\mathcal{E}}_h$, a unit normal vector $\mathbf{n}_e$ is associated. Two elements sharing the common edge e are denoted as T_e^1 and T_e^2, where $\mathbf{n}_e$ points from T_e^1 to T_e^2. For a vector-valued function $\mathbf{g}$, the jump operator $[\![\cdot]\!]_e$ and average operator $\{\!\{\cdot\}\!\}_e$ across an edge e are defined as follows.

$$[\![\mathbf{g}]\!]_e = (\mathbf{g}|_{T_e^1})|_e - (\mathbf{g}|_{T_e^2})|_e, \quad \{\!\{\mathbf{g}\}\!\}_e = \frac{1}{2}\left((\mathbf{g}|_{T_e^1})|_e + (\mathbf{g}|_{T_e^2})|_e\right). \tag{2.9}$$

Lastly, we adopt the following assumptions [35] to characterize the geometrical relations between the mesh and the interface.

(H1) The interface Γ cannot intersect an edge of any element at more than two points unless the edge is part of Γ.
(H2) If Γ intersects the boundary of an element at two points, these intersection points must be on different edges of this element.
(H3) The interface Γ is a piecewise C^2 function, and the mesh $\mathcal{T}_h$ is formed such that on every interface element $T \in \mathcal{T}_h^i$, $\Gamma \cap T$ is C^2.

2.2. IFE spaces for elasticity problem

In this subsection, we recall the linear and bilinear IFE spaces [25]. To unify the notations, we define the index set $\mathcal{I}_T$ for each element $T \in \mathcal{T}_h$ such that $\mathcal{I}_T = \{1, 2, 3\}$ for triangular elements, and $\mathcal{I}_T = \{1, 2, 3, 4\}$ for rectangular elements.

On non-interface elements $T \in \mathcal{T}_h^n$, we use the standard vector-valued polynomial space. The local finite element space is $\mathbf{S}_h(T) = \mathcal{P}_1(T) \times \mathcal{P}_1(T)$ for triangular mesh and $\mathbf{S}_h(T) = \mathcal{Q}_1(T) \times \mathcal{Q}_1(T)$ for rectangular mesh. On an interface element $T \in \mathcal{T}_h^i$, based on **(H2)**, we assume the interface Γ intersects boundary of T at two points D and E, located on two different edges. The vector $\mathbf{n}_{\overline{DE}}$ is the unit normal of the line segment $\Gamma_T = \overline{DE}$. Then the interface element T is split into $\widetilde{T}^+$ and $\widetilde{T}^-$ by Γ_T. Typical interface elements with notations defined above are illustrated in Fig. 2.

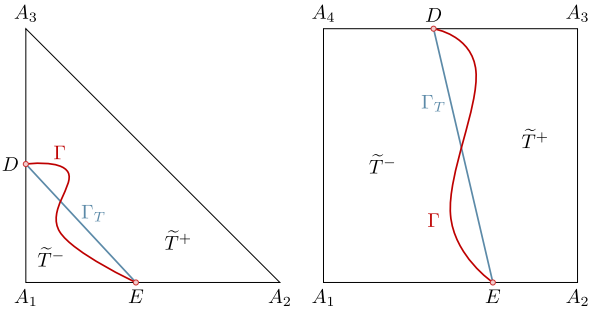

Fig. 2. Typical triangular (left) and rectangular (right) interface elements.

We construct the local basis functions $\boldsymbol{\phi}_{i,T}$, $i = 1, 2, \cdots, 2|\mathcal{I}_T|$ on the interface element as follows

$$\boldsymbol{\phi}_{i,T}(\mathbf{x}) = \begin{cases} \boldsymbol{\phi}^+_{i,T}(\mathbf{x}) = \begin{pmatrix} a_1^+ + b_1^+ x + c_1^+ y \\ a_2^+ + b_2^+ x + c_2^+ y \end{pmatrix}, & \text{if } \mathbf{x} \in \widetilde{T}^+, \\ \boldsymbol{\phi}^-_{i,T}(\mathbf{x}) = \begin{pmatrix} a_1^- + b_1^- x + c_1^- y \\ a_2^- + b_2^- x + c_2^- y \end{pmatrix}, & \text{if } \mathbf{x} \in \widetilde{T}^-, \end{cases} \tag{2.10}$$

for linear case on triangular meshes, and

$$\boldsymbol{\phi}_{i,T}(\mathbf{x}) = \begin{cases} \boldsymbol{\phi}^+_{i,T}(\mathbf{x}) = \begin{pmatrix} a_1^+ + b_1^+ x + c_1^+ y + d_1^+ xy \\ a_2^+ + b_2^+ x + c_2^+ y + d_2^+ xy \end{pmatrix}, & \text{if } \mathbf{x} \in \widetilde{T}^+, \\ \boldsymbol{\phi}^-_{i,T}(\mathbf{x}) = \begin{pmatrix} a_1^- + b_1^- x + c_1^- y + d_1^- xy \\ a_2^- + b_2^- x + c_2^- y + d_2^- xy \end{pmatrix}, & \text{if } \mathbf{x} \in \widetilde{T}^-, \end{cases} \tag{2.11}$$

for bilinear case on rectangular meshes. These IFE basis functions satisfy the standard nodal value conditions;

$$\boldsymbol{\phi}_{i,T}(A_j) = \begin{bmatrix} \delta_{i,j} \\ 0 \end{bmatrix}, \forall i = 1, ..., |\mathcal{I}_T|, \quad \boldsymbol{\phi}_{i,T}(A_j) = \begin{bmatrix} 0 \\ \delta_{i-|\mathcal{I}_T|,j} \end{bmatrix}, \forall i = |\mathcal{I}_T| + 1, \cdots, 2|\mathcal{I}_T|. \tag{2.12}$$

Besides, we enforce the interface conditions (1.1h)-(1.1i) approximately as follows:

- Continuity of displacement functions

$$\boldsymbol{\phi}^+_{i,T}|_{\Gamma_T} - \boldsymbol{\phi}^-_{i,T}|_{\Gamma_T} = \mathbf{0}, \tag{2.13}$$

- Continuity of stress in normal direction

$$\big(\sigma(\boldsymbol{\phi}^+_{i,T}(F)) - \sigma(\boldsymbol{\phi}^-_{i,T}(F))\big)\mathbf{n}_{\overline{DE}} = \mathbf{0}, \tag{2.14}$$

where F is taken to be $(D + E)/2$ as in [35] or as a weighted average of D and E as in [17].

The local IFE space $\mathbf{S}_h(T)$ on an interface element $T \in \mathcal{T}_h^i$ is defined as $\mathbf{S}_h(T) \triangleq \text{Span}\{\boldsymbol{\phi}_{i,T} : 1 \le i \le 2|\mathcal{I}_T|\}$. The global IFE space $\mathbf{S}_h(\Omega)$ is defined to be

$$\mathbf{S}_h(\Omega) = \{\mathbf{v} : \mathbf{v}|_T \in \mathbf{S}_h(T), \forall T \in \mathcal{T}_h; \mathbf{v} \text{ is continuous at each node } N \in \mathcal{N}_h; \mathbf{v}|_{\partial\Omega} = \mathbf{0}\}. \tag{2.15}$$

We will sometimes just denote the global space $\mathbf{S}_h(\Omega)$ by $\mathbf{S}_h$ for convenience. It is clear that $\mathbf{S}_h$ is a subspace of $\mathbf{V}_h$ where

$$\mathbf{V}_h = \{\mathbf{v} : \ \mathbf{v}|_T \in [H^1(T)]^2, \forall T \in \mathcal{T}_h; \mathbf{v} \text{ is continuous at each node } N \in \mathcal{N}_h, \mathbf{v} \text{ is continuous across each } e \in \mathring{\mathcal{E}}_h^n, \mathbf{v}|_{\partial\Omega} = \mathbf{0}\}. \tag{2.16}$$

More detail on the construction of the IFE spaces for elasticity problems and their properties can be found in [17,35].

3. Semi-discrete and fully discrete numerical schemes

In this section, we introduce the IFE discretization for elastodynamic interface problem (1.1).

3.1. Spatial discretization

In this subsection, we introduce the spatial discretization using the IFE spaces defined above. We use the partially penalized IFE scheme introduced in [18]. Define the following bilinear and linear forms:

$$\begin{aligned} a_h(\mathbf{u}, \mathbf{v}) = &\sum_{T \in \mathcal{T}_h} \int_T 2\mu\epsilon(\mathbf{u}) : \epsilon(\mathbf{v}) d\mathbf{x} + \sum_{T \in \mathcal{T}_h} \int_T \lambda(\nabla \cdot \mathbf{u})(\nabla \cdot \mathbf{v}) d\mathbf{x} \\ &- \sum_{e \in \mathring{\mathcal{E}}_h^i} \int_e \{\{\sigma(\mathbf{u})\mathbf{n}_e\}\} \cdot [\![\mathbf{v}]\!] \, ds - \sum_{e \in \mathring{\mathcal{E}}_h^i} \int_e \{\{\sigma(\mathbf{v})\mathbf{n}_e\}\} \cdot [\![\mathbf{u}]\!] \, ds + \frac{\rho}{h} \sum_{e \in \mathring{\mathcal{E}}_h^i} \int_e [\![\mathbf{u}]\!] \cdot [\![\mathbf{v}]\!] \, ds, \end{aligned} \tag{3.1}$$

$$L_{\mathbf{f}}(\mathbf{v}) = \sum_{T\in\mathcal{T}_h}\int_T \mathbf{f}\cdot\mathbf{v}d\mathbf{x}, \tag{3.2}$$

where $\rho>0$ is a penalty parameter. The variational form for the elastodynamics problem (1.1) is: find $\mathbf{u}\in H^2(0,L;\mathbf{PH}^2(\Omega))$ such that

$$(\mathbf{u}_{tt},\mathbf{v}) + a_h(\mathbf{u},\mathbf{v}) = L_{\mathbf{f}}(\mathbf{v}), \qquad \forall \mathbf{v}\in\mathbf{V}_h,\ t>0, \tag{3.3a}$$

$$\mathbf{u}(0)=\boldsymbol{\omega}_0, \qquad \mathbf{u}_t(0)=\boldsymbol{\omega}_1. \tag{3.3b}$$

The semi-discrete scheme for (1.1) is: find $\mathbf{u}_h\in H^2(0,L;\mathbf{S}_h)$ such that

$$(\mathbf{u}_{h,tt},\mathbf{v}_h) + a_h(\mathbf{u}_h,\mathbf{v}_h) = L_{\mathbf{f}}(\mathbf{v}_h), \qquad \forall \mathbf{v}_h\in\mathbf{S}_h,\ t>0, \tag{3.4a}$$

$$\mathbf{u}_h(0)=\mathcal{R}_h\boldsymbol{\omega}_0, \qquad \mathbf{u}_{h,t}(0)=\mathcal{R}_h\boldsymbol{\omega}_1, \tag{3.4b}$$

where the elastic projection operator $\mathcal{R}_h$: $\mathbf{V}_h\mapsto\mathbf{S}_h$ is defined by

$$a_h(\mathcal{R}_h\boldsymbol{\omega},\mathbf{v}_h) = a_h(\boldsymbol{\omega},\mathbf{v}_h), \qquad \forall \mathbf{v}_h\in\mathbf{S}_h. \tag{3.5}$$

We define the mesh-dependent energy norm $|||\cdot|||_h$:

$$|||\mathbf{v}|||_h^2 := \sum_{T\in\mathcal{T}_h}\int_T 2\mu\|\epsilon(\mathbf{v})\|^2 d\mathbf{x} + \sum_{T\in\mathcal{T}_h}\int_T \lambda\|\nabla\cdot\mathbf{v}\|^2 d\mathbf{x} + \sum_{e\in\mathcal{E}_h^i}\rho\int_e \|h^{-1/2}[\![\mathbf{v}]\!]\|^2 ds + \sum_{e\in\mathcal{E}_h^i}\rho^{-1}\int_e \|h^{1/2}\{\{\sigma(\mathbf{v})\mathbf{n}_e\}\}\|^2 ds. \tag{3.6}$$

The following approximation property has been proved in Theorem 4.3 of [18]:

Lemma 3.1. *For every $\mathbf{u}\in\mathbf{PH}^2(\Omega)$, assume ρ sufficiently large, then $\mathcal{R}_h u$ is well-defined and the following estimate holds:*

$$|||\mathbf{u}-\mathcal{R}_h\mathbf{u}|||_h \lesssim h\,\|\mathbf{u}\|_{\mathbf{PH}^2(\Omega)}, \tag{3.7a}$$

$$\|\mathbf{u}-\mathcal{R}_h\mathbf{u}\|_{\mathbf{L}^2(\Omega)} \lesssim h^2\,\|\mathbf{u}\|_{\mathbf{PH}^2(\Omega)}, \tag{3.7b}$$

$$|\mathbf{u}-\mathcal{R}_h\mathbf{u}|_{\mathbf{PH}^1(\Omega)} \lesssim h\,\|\mathbf{u}\|_{\mathbf{PH}^2(\Omega)}. \tag{3.7c}$$

Here and in what follows, the notation $u\lesssim v$ denotes $u\le Cv$ where the hidden constant C is independent of the mesh size h and the interface location. The proof for the energy norm (3.7a) and the L^2 norm (3.7b) is reported in [18]. The H^1 norm error estimate (3.7c) is a direct consequence by combining the H^1 estimate for Lagrange interpolation error $|\mathbf{u}-\mathcal{I}_h\mathbf{u}|_{H^1}$ in [17] and the inverse inequality in Theorem 4.1 in this paper.

3.2. Temporal discretization

In the subsection, we further discretize the scheme (3.4) in time. Let $\mathcal{P}_\tau$ be a uniform partition of the time domain $[0,L]$ with the step size τ:

$$\mathcal{P}_\tau = \{0=t^0<t^1<\cdots<t^M=L\},\ \tau=t^n-t^{n-1}, n=1,2,...,M. \tag{3.8}$$

For a vector function $\mathbf{v}(\mathbf{x},t)$, we denote $\mathbf{v}^n := \mathbf{v}(\cdot,t^n)$ and define the following difference functions:

$$\begin{aligned} &\partial_{tt}\mathbf{v}^n := \frac{\mathbf{v}^{n+1}-2\mathbf{v}^n+\mathbf{v}^{n-1}}{\tau^2}, \qquad \partial_t\mathbf{v}^{n+1/2} := \frac{\mathbf{v}^{n+1}-\mathbf{v}^n}{\tau},\\ &\mathbf{v}^{n,\theta} := \theta\mathbf{v}^{n+1}+(1-2\theta)\mathbf{v}^n+\theta\mathbf{v}^{n-1}, \quad \mathbf{v}^{n+\theta} := \theta\mathbf{v}^{n+1}+(1-\theta)\mathbf{v}^n, \end{aligned} \tag{3.9}$$

where $\theta\in[0,1]$. The fully discretized scheme for (1.1) is: find $\mathbf{u}_h^n$ for $n=2,3,\cdots,M$ in

$$(\partial_{tt}\mathbf{u}_h^n,\mathbf{v}_h) + a_h(\mathbf{u}_h^{n,1/4},\mathbf{v}_h) = L_{\mathbf{f}^{n,1/4}}(\mathbf{v}_h), \qquad \forall \mathbf{v}_h\in\mathbf{S}_h, \tag{3.10a}$$

$$\mathbf{u}_h^0=\mathcal{R}_h\boldsymbol{\omega}_0, \qquad \mathbf{u}_h^1=\mathcal{R}_h\mathbf{u}^{1,*}, \tag{3.10b}$$

where, $\mathbf{u}^{1,*}=\boldsymbol{\omega}_0+\tau\boldsymbol{\omega}_1+\frac{\tau^2}{2}(\mathrm{div}\,\sigma(\boldsymbol{\omega}_0)+\mathbf{f}(\mathbf{x},0))$ is a third-order approximation of $\mathbf{u}^1$. The matrix form of the above fully discrete scheme can be written as:

$$(\mathbf{M}+\frac{\tau^2}{4}\mathbf{K})\mathbf{c}^{n+1} = (2\mathbf{M}-\frac{\tau^2}{2}\mathbf{K})\mathbf{c}^n - (\mathbf{M}+\frac{\tau^2}{4}\mathbf{K})\mathbf{c}^{n-1} + \tau^2\mathbf{F}^{n,1/4}. \tag{3.11}$$

Here, $\mathbf{c}^n$ is the vector of unknowns. $(\mathbf{M})_{i,j}=(\boldsymbol{\phi}_i,\boldsymbol{\phi}_j)$, $(\mathbf{K})_{i,j}=a_h(\boldsymbol{\phi}_i,\boldsymbol{\phi}_j)$ are mass and stiffness matrices, and $(\mathbf{F}^{n,1/4})_i=L_{\mathbf{f}^{n,1/4}}(\boldsymbol{\phi}_i)$ is the load vector.

Remark 3.1. In [31], the fully discrete scheme is called θ-scheme. In our paper, we use θ-scheme for temporal discretization with $\theta=1/4$.

4. Error estimation

In this section, we derive the *a priori* error estimation for both semi-discrete and fully discrete schemes. First we prove some inverse inequalities for IFE functions.

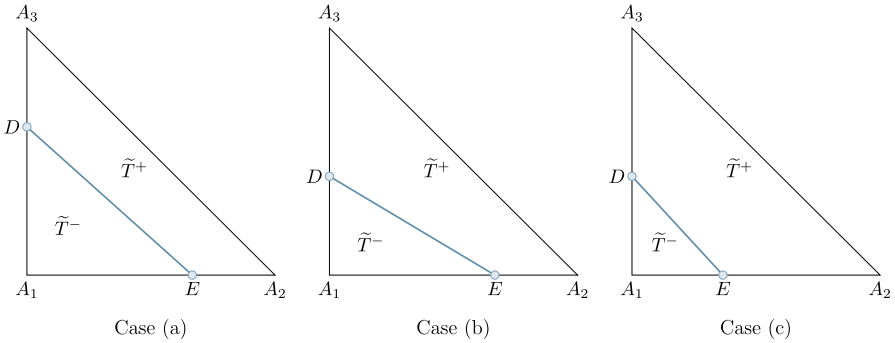

Fig. 3. Three typical cases for triangular interface elements.

4.1. Inverse inequalities

We first recall the following norm equivalence lemma for triangular meshes [16].

Lemma 4.1. *Let $T \in \mathcal{T}_h^i$ be an interface triangle in one of three cases illustrated in Fig. 3. Let $\mathcal{P}_k$ be the polynomial space of degree no more than k, then the following norm equivalent results hold*

- *For Case (a): $|A_1E| \geq |A_1A_2|/2$ and $|A_1D| \geq |A_1A_3|/2$, we have*

$$\|\cdot\|_{L^2(\widetilde{T}^-)} \simeq \|\cdot\|_{L^2(T)}, \quad \text{on } \mathcal{P}_k. \tag{4.1}$$

- *For Case (b): $|A_1E| \geq |A_1A_2|/2$ and $|A_1D| \leq |A_1A_3|/2$ and Case (c): $|A_1E| \leq |A_1A_2|/2$ and $|A_1D| \leq |A_1A_3|/2$, we have*

$$\|\cdot\|_{L^2(\widetilde{T}^+)} \simeq \|\cdot\|_{L^2(T)}, \quad \text{on } \mathcal{P}_k. \tag{4.2}$$

An analogous norm equivalence result can be established for rectangular interface elements.

Lemma 4.2. *Let $T \in \mathcal{T}_h^i$ be an interface rectangle in one of three cases illustrated in Fig. 4. Let $\mathcal{P}_k$ be the polynomial space of degree no more than k, then the following norm equivalent results hold*

- *For Case (d): $D \in A_1A_4$ and $E \in A_1A_2$, we have*

$$\|\cdot\|_{L^2(\widetilde{T}^+)} \simeq \|\cdot\|_{L^2(T)}, \quad \text{on } \mathcal{P}_k. \tag{4.3}$$

- *For Case (e): $|A_1E| \geq |A_1A_2|/2$ and $|A_4D| \geq |A_4A_3|/2$ and Case (f): $|A_1E| \geq |A_1A_2|/2$ and $|A_4D| \leq |A_4A_3|/2$, we have*

$$\|\cdot\|_{L^2(\widetilde{T}^-)} \simeq \|\cdot\|_{L^2(T)}, \quad \text{on } \mathcal{P}_k. \tag{4.4}$$

Proof. For Case (d), we let M, N be the midpoint of A_3A_4 and A_2A_3, and let O be the center of square. It is clear that the rectangle ONA_3M is a homothetic subset of T. By Lemma 2.2 in [46], we have

$$\|v\|_{L^2(\widetilde{T}^+)} \leq \|v\|_{L^2(T)} \lesssim \|v\|_{L^2(\square ONA_3M)} \leq \|v\|_{L^2(\widetilde{T}^+)}, \qquad \forall v \in \mathcal{P}_k,$$

where the hidden constant in the estimate depends only on k, the order of polynomial.

For Case (e), we let M, N be the mid-point of A_1A_4 and A_1A_2, and let O be the center of T. A similar argument yields

$$\|v\|_{L^2(\widetilde{T}^-)} \leq \|v\|_{L^2(T)} \lesssim \|v\|_{L^2(\square ONA_1M)} \leq \|v\|_{L^2(\widetilde{T}^-)} \qquad \forall v \in \mathcal{P}_k.$$

For Case (f), we let M and N be the first quadrisection point of A_1A_4 and A_1A_2, respectively. Let O be the fourth point of $\square ONA_1M$. A similar argument yields

$$\|v\|_{L^2(\widetilde{T}^-)} \leq \|v\|_{L^2(T)} \lesssim \|v\|_{L^2(\square ONA_1M)} \leq \|v\|_{L^2(\widetilde{T}^-)} \qquad \forall v \in \mathcal{P}_k.$$

This completes the proof of the lemma. □

Recall the standard trace inequalities [45] in 1D and 2D cases:

$$|v(z)| \leqslant \frac{k+1}{\sqrt{|I|}} \|v\|_{L^2(I)}, \quad \forall v \in \mathcal{P}_k(I) \tag{4.5}$$

where I is a line segment, and z is an endpoint of I. Moreover,

$$\|v\|_{L^2(e)} \leqslant \sqrt{\frac{(k+1)(k+2)}{2} \frac{|e|}{|T|}} \|v\|_{L^2(T)}, \quad \forall v \in \mathcal{P}_k(T) \tag{4.6}$$

where T is a triangle and e is an edge of T.

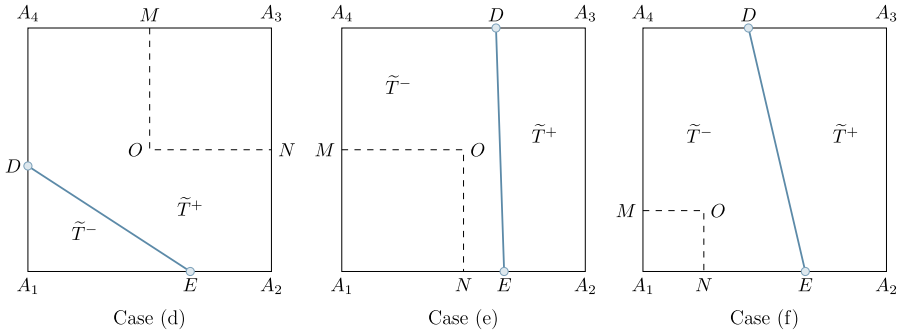

Fig. 4. Three typical cases for rectangular interface elements.

We also recall from [17], an IFE function $\boldsymbol{\phi}_T$ can be written as

$$\boldsymbol{\phi}_T = \begin{cases} \boldsymbol{\phi}_T^+ = \mathbf{p} & \text{in } \widetilde{T}^+ \\ \boldsymbol{\phi}_T^- = \mathcal{M}_T(\mathbf{p}) & \text{in } \widetilde{T}^- \end{cases}$$

where $\mathbf{p}$ is a polynomial in $[\mathcal{P}_1(T)]^2$ for linear case while in $[\mathcal{Q}_1(T)]^2$ for bilinear case and $\mathcal{M}_T(\mathbf{p}) = \mathbf{p} + \mathbf{c}_0^- L(X)$ is the extension mapping with $L(X) = \widetilde{\mathbf{n}}(X - D)$ and $\widetilde{\mathbf{n}}$ is the unit normal vector of $\overline{DE}$. It is clear that $L(X)$ is the equation of the line segment $\overline{DE}$. By direct calculation, we have

$$\mathbf{c}_0^- = (K^-)^{-1}\hat{\sigma}(\boldsymbol{\phi}_T^+)(F)\widetilde{\mathbf{n}} \tag{4.7}$$

where $\hat{\sigma}(\mathbf{v}) = \left(\hat{\sigma}_{ij}(\mathbf{v})\right)_{1\leqslant i,j\leqslant 2}$ and

$$\hat{\sigma}_{ij}(\mathbf{v}) = \hat{\lambda}(\nabla\cdot\mathbf{v})\delta_{i,j} + 2\hat{\mu}\epsilon_{ij}(\mathbf{v}), \tag{4.8}$$

with $\hat{\lambda} = \lambda^+ - \lambda^-$ and $\hat{\mu} = \mu^+ - \mu^-$. The matrix $K^- = QP^-Q^T$ where

$$P^- = \begin{bmatrix} (\lambda^- + 2\mu^-) & 0 \\ 0 & \mu^- \end{bmatrix}, \quad Q = [\widetilde{\mathbf{n}}, \widetilde{\mathbf{t}}] \tag{4.9}$$

with $\widetilde{\mathbf{t}}$ being the unit tangential vector of $\overline{DE}$. It can be also verified by switching the signs between $-$ to $+$ that $\mathcal{M}_T^{-1}(\mathbf{p}) = \mathbf{p} + \mathbf{c}_0^+ L(X)$ where $\mathbf{c}_0^+$ is defined similarly to $\mathbf{c}_0^-$. These results will be used to prove the inverse inequality in the next theorem.

Theorem 4.1 *(Inverse Inequality). The following estimate holds for each interface element $T \in \mathcal{T}_h^i$,*

$$\left\|\nabla\boldsymbol{\phi}_T\right\|_{L^2(T)} \lesssim h^{-1}\left\|\boldsymbol{\phi}_T\right\|_{L^2(T)}, \quad \forall\boldsymbol{\phi}_T \in \mathbf{S}_h(T). \tag{4.10}$$

Proof. Without loss of generality, we consider the three cases of triangular elements specified in Fig. 3. Note that

$$\|L(X)\|_{L^2(\widetilde{T}^s)} = \left\|\widetilde{\mathbf{n}}(X - D)\right\|_{L^2(\widetilde{T}^s)} \lesssim \|(X - D)\|_{L^2(\widetilde{T}^s)} \lesssim h|\widetilde{T}^s|^{1/2} \lesssim h^2, \quad s = +, -. \tag{4.11}$$

In addition, we can bound $(K^s)^{-1}$ as follows

$$\left\|(K^s)^{-1}\right\| \lesssim \left\|Q^T\right\| \left\|(P^s)^{-1}\right\| \|Q\| \lesssim 1, \quad s = +, -. \tag{4.12}$$

For Case (a) in Lemma 4.1, by the standard inverse inequality and the norm equivalence results, we have

$$\left\|\nabla\boldsymbol{\phi}_T^-\right\|_{L^2(\widetilde{T}^-)} \leq \left\|\nabla\boldsymbol{\phi}_T^-\right\|_{L^2(T)} \lesssim h^{-1}\left\|\boldsymbol{\phi}_T^-\right\|_{L^2(T)} \lesssim h^{-1}\left\|\boldsymbol{\phi}_T^-\right\|_{L^2(\widetilde{T}^-)}. \tag{4.13}$$

Similarly, we can bound the other piece as follows

$$\left\|\nabla\boldsymbol{\phi}_T^+\right\|_{L^2(\widetilde{T}^+)} \leq \left\|\nabla\boldsymbol{\phi}_T^+\right\|_{L^2(T)} \lesssim h^{-1}\left\|\boldsymbol{\phi}_T^+\right\|_{L^2(T)} = h^{-1}\left\|\boldsymbol{\phi}_T^+\right\|_{L^2(\widetilde{T}^+)} + h^{-1}\left\|\boldsymbol{\phi}_T^+\right\|_{L^2(\widetilde{T}^-)}. \tag{4.14}$$

Using the triangle inequality we obtain

$$\begin{aligned} h^{-1}\left\|\boldsymbol{\phi}_T^+\right\|_{L^2(\widetilde{T}^+)} + h^{-1}\left\|\boldsymbol{\phi}_T^+\right\|_{L^2(\widetilde{T}^-)} &\leq h^{-1}\left\|\boldsymbol{\phi}_T^+\right\|_{L^2(\widetilde{T}^+)} + h^{-1}\left\|\boldsymbol{\phi}_T^-\right\|_{L^2(\widetilde{T}^-)} + h^{-1}\left\|\boldsymbol{\phi}_T^+ - \boldsymbol{\phi}_T^-\right\|_{L^2(\widetilde{T}^-)} \\ &= h^{-1}\left\|\boldsymbol{\phi}_T\right\|_{L^2(T)} + h^{-1}\left\|\mathbf{c}_0^+ L\right\|_{L^2(\widetilde{T}^-)}. \end{aligned} \tag{4.15}$$

Note that $\mathbf{c}_0^+$ in second term on the right hand side of (4.15) is a constant function of X. By (4.11), (4.12), the trace inequality (4.5) applied on $\overline{DF}$, we obtain

$$\begin{aligned} \left\|\mathbf{c}_0^+ L\right\|_{L^2(\widetilde{T}^-)} &\leq \left\|\mathbf{c}_0^+\right\|_{L^2(\widetilde{T}^-)} \|L\|_{L^2(\widetilde{T}^-)} \lesssim h^2|\hat{\sigma}(\boldsymbol{\phi}_T^-)(F)| \\ &\lesssim h^2|DF|^{-1/2}\left\|\hat{\sigma}(\boldsymbol{\phi}_T^-)\right\|_{L^2(DF)} \lesssim h^2|DE|^{-1/2}\left\|\hat{\sigma}(\boldsymbol{\phi}_T^-)\right\|_{L^2(DE)}. \end{aligned} \tag{4.16}$$

In the last inequality, we used the assumption $|DF| \geq |DE|/2$. Note that $|\triangle A_1 DE| \geq h^2/8$, then applying the standard trace and inverse inequalities on $\triangle A_1 DE$ we have

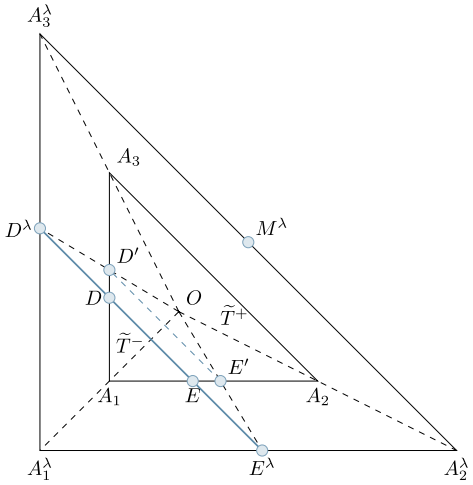

Fig. 5. An illustration of a fictitious triangular element of Case (c).

$$\left\|\mathbf{c}_0^+ L\right\|_{L^2(\widetilde{T}^-)} \lesssim h^2 h^{-1} \left\|\hat{\sigma}(\boldsymbol{\phi}_T^-)\right\|_{L^2(\triangle A_1 DE)} \lesssim h \left\|\nabla \boldsymbol{\phi}_T^-\right\|_{L^2(\triangle A_1 DE)} \lesssim \left\|\boldsymbol{\phi}_T^-\right\|_{L^2(\widetilde{T}^-)} \leq \|\boldsymbol{\phi}_T\|_{L^2(T)}. \tag{4.17}$$

This proves the Case (a). The proof of Case (b) is similar to Case (a) with the fact that $|\triangle A_3 DE| \geq h^2/8$ and $|DE| \geq \sqrt{2}h/2$.

For Case (c), note that $|DE|$ can be arbitrarily small; hence, we apply the idea of the fictitious element stated in [49]. The fictitious element is only used for proof but not in the actual computation. Let O be the barycenter of $\triangle A_1 A_2 A_3$, then we define the homothetic transformation of T with respect to O to be T_λ denoted by $\triangle A_1^\lambda A_2^\lambda A_3^\lambda$ which satisfies $T_\lambda = \{X \in \mathbb{R}^2 : \exists Y \in T \text{ s.t. } \overrightarrow{OX} = \lambda \overrightarrow{OY}\}$. The line DE intersects T_λ with D^λ and E^λ. We also denote D' and E' to be the homothetic pre-image of D^λ and E^λ. See Fig. 5 for an illustration. Then we can prove for the one piece $\widetilde{T}^+$ by norm equivalence (4.1) and (4.2):

$$\left\|\nabla \boldsymbol{\phi}_T^+\right\|_{L^2(\widetilde{T}^+)} \leq \left\|\nabla \boldsymbol{\phi}_T^+\right\|_{L^2(T)} \lesssim h^{-1} \left\|\boldsymbol{\phi}_T^+\right\|_{L^2(T)} \lesssim h^{-1} \left\|\boldsymbol{\phi}_T^+\right\|_{L^2(\widetilde{T}^+)}. \tag{4.18}$$

For the other piece, we have

$$\begin{aligned} \left\|\nabla \boldsymbol{\phi}_T^-\right\|_{L^2(\widetilde{T}^-)} &\leq \left\|\nabla \boldsymbol{\phi}_T^-\right\|_{L^2(T)} \lesssim h^{-1} \left\|\boldsymbol{\phi}_T^-\right\|_{L^2(T)} = h^{-1} \left(\left\|\boldsymbol{\phi}_T^-\right\|_{L^2(\widetilde{T}^-)} + \left\|\boldsymbol{\phi}_T^-\right\|_{L^2(\widetilde{T}^+)} \right) \\ &\lesssim h^{-1} \left(\|\boldsymbol{\phi}_T\|_{L^2(T)} + \left\|\mathbf{c}_0^- L\right\|_{L^2(\widetilde{T}^+)} \right). \end{aligned} \tag{4.19}$$

Then, by (4.11), (4.12), and the trace inequality (4.5) applied on $D^\lambda F$, we obtain:

$$\left\|\mathbf{c}_0^- L\right\|_{L^2(\widetilde{T}^+)} \lesssim h^2 |\hat{\sigma}(\boldsymbol{\phi}_T^+)(F)| \lesssim h^2 |D^\lambda E^\lambda|^{-1/2} \left\|\hat{\sigma}(\boldsymbol{\phi}_T^+)\right\|_{L^2(D^\lambda E^\lambda)}. \tag{4.20}$$

Here we used the assumption $|D^\lambda F| \geq 1/2 |D^\lambda E^\lambda|$. Let M^λ be the midpoint of $A_2^\lambda A_3^\lambda$ and note that $|\triangle D^\lambda M^\lambda E^\lambda| \geq 1/9(\lambda - 1)^2 h^2$. We then take a fixed value $\lambda > 1$, apply the standard trace inequality, inverse inequality on $\triangle D^\lambda E^\lambda M^\lambda$, and note that $D' E' A_2 A_3$ is the homothetic subset of $D^\lambda E^\lambda A_2^\lambda A_3^\lambda$ to get:

$$\begin{aligned} \left\|\mathbf{c}_0^- L\right\|_{L^2(\widetilde{T}^+)} &\lesssim h \left\|\hat{\sigma}(\boldsymbol{\phi}_T^+)\right\|_{L^2(\triangle D^\lambda E^\lambda M^\lambda)} \lesssim h \left\|\nabla \boldsymbol{\phi}_T^+\right\|_{L^2(\triangle D^\lambda E^\lambda M^\lambda)} \lesssim \left\|\boldsymbol{\phi}_T^+\right\|_{L^2(\triangle D^\lambda E^\lambda M^\lambda)} \\ &\lesssim \left\|\boldsymbol{\phi}_T^+\right\|_{L^2(D^\lambda E^\lambda A_2^\lambda A_3^\lambda)} \lesssim \left\|\boldsymbol{\phi}_T^+\right\|_{L^2(D' E' A_2 A_3)} \lesssim \left\|\boldsymbol{\phi}_T^+\right\|_{L^2(\widetilde{T}^+)} \lesssim \|\boldsymbol{\phi}_T\|_{L^2(T)}. \end{aligned} \tag{4.21}$$

Here we used Lemma 2.2 of [46] again. This finishes the proof of Case (c) of triangular interface elements.

For rectangular elements, Case (e) and Case (f) are proved in a similar procedure with (a) and (b). For Case (d), we decompose $\square A_1 A_2 A_3 A_4$ into $\triangle A_1 A_2 A_4$ and $\triangle A_2 A_3 A_4$, then repeat the argument as in triangular elements on $\triangle A_1 A_2 A_4$ and use the standard inverse inequality on $\triangle A_2 A_3 A_4$. $\square$

Remark 4.1. The proof of triangular elements in Lemma 4.1 and Theorem 4.1 is based on equilateral right triangle element shape in the proof. The results hold valid for general triangular elements by the standard affine mapping.

Recall the following coercivity and continuity results for $a_h(\cdot,\cdot)$ which have been proved in [18]:

$$|||\mathbf{v}_h|||_h^2 \lesssim a_h(\mathbf{v}_h, \mathbf{v}_h) \lesssim |||\mathbf{v}_h|||_h^2, \quad \forall \mathbf{v}_h \in \mathbf{S}_h. \tag{4.22}$$

The following relationship between the energy norm and the L^2 norm is established.

Lemma 4.3. *The following inequality holds:*

$$\|\mathbf{u}\|_{L^2(\Omega)} \lesssim |||\mathbf{u}|||_h, \quad \forall \mathbf{u} \in \mathbf{V}_h. \tag{4.23}$$

Proof. Applying Poincaré-Friedrichs' inequality for piecewise H^1 space [3], Korn's inequality for piecewise H^1 space [4] and definition of $|||\cdot|||_h$, for any function $\mathbf{u} \in \mathbf{V}_h$:

$$\|\mathbf{u}\|^2_{L^2(\Omega)} \lesssim \|\nabla \mathbf{u}\|^2_{L^2(\Omega)} + \sum_{e\in\mathring{\mathcal{E}}_h^i} \int_e \|h^{-1/2}\,[\![\mathbf{v}]\!]\,\|^2 ds \lesssim \|\epsilon(\mathbf{u})\|^2_{L^2(\Omega)} + \sum_{e\in\mathring{\mathcal{E}}_h^i} \int_e \|h^{-1/2}\,[\![\mathbf{v}]\!]\,\|^2 ds \lesssim |||\mathbf{u}|||_h^2. \quad \square \tag{4.24}$$

For each element $T \in \mathcal{T}_h$, we define the patch $\omega_T = \cup \left\{ T' \in \mathcal{T}_h : \overline{T'} \cap \overline{T} \neq \emptyset \right\}$. The following the patch assumption [22,18] holds true: for every interface element $T \in \mathcal{T}_h^i$ and an interface edge e of T, each sub-edge $e^s = e \cap \Omega^s$, $s = +, -$, there exists a triangle $K_e^s \subset \Omega^s \cap \omega_T$ such that e^s is one of edges of this triangle such that

$$h|e^s| \lesssim |K_e^s| \lesssim h|e^s|. \tag{4.25}$$

This assumption will be used to prove the global trace inequality [18].

Lemma 4.4. *Assume that the mesh $\mathcal{T}_h$ satisfies the patch assumption. Then the following trace inequality holds:*

$$\sum_{e\in\mathring{\mathcal{E}}_h^i} \left\| \{\{ h^{1/2}\sigma(\mathbf{u})\mathbf{n}_e \}\} \right\|_{L^2(e)} \lesssim \|\mathbf{u}\|_{\mathbf{PH}^2(\Omega)}, \quad \forall \mathbf{u} \in \mathbf{PH}^2(\Omega). \tag{4.26}$$

Proof. For each interface edge $e \in \mathcal{E}_h^i$, we denote its segments $e^s = e \cap \Omega^s$, $s = +, -$. Following the patch assumption (4.25), for each edge segment e^s, there exists a triangle $K_e^s \subset \omega_T$ such that it satisfies $|e^s| \lesssim h^{-1}|K_e^s|$. Then we use the standard trace inequality on K_e^s and obtain the following estimates:

$$\begin{aligned} \|h^{1/2}\sigma(\mathbf{u})\mathbf{n}_e\|_{L^2(e)} &\lesssim h^{1/2}(\|\nabla \mathbf{u}\|_{L^2(e^+)} + \|\nabla \mathbf{u}\|_{L^2(e^-)}) \\ &\lesssim h^{1/2} \sum_{s=+,-} \left(|e^s|/|K_e^s| \right)^{1/2} (\|\nabla \mathbf{u}\|_{L^2(K_e^s)} + h\|\nabla^2 \mathbf{u}\|_{L^2(K_e^s)}) \\ &= \sum_{s=\pm} (\|\nabla \mathbf{u}\|_{L^2(K_e^s)} + h\|\nabla^2 \mathbf{u}\|_{L^2(K_e^s)}). \end{aligned} \tag{4.27}$$

Summing (4.27) over $e \in \mathring{\mathcal{E}}_h^i$ we obtain:

$$\begin{aligned} \sum_{e\in\mathring{\mathcal{E}}_h^i} \left\| \{\{ h^{1/2}\sigma(\mathbf{u})\mathbf{n}_e \}\} \right\|_{L^2(e)} &\lesssim \sum_{e\in\mathring{\mathcal{E}}_h^i} \sum_{s=+,-} (\|\nabla \mathbf{u}\|_{L^2(K_e^s)} + h\|\nabla^2 \mathbf{u}\|_{L^2(K_e^s)}) \\ &\lesssim \sum_{T\in\mathcal{T}_h} \|\mathbf{u}\|_{\mathbf{PH}^2(\omega_T)} \lesssim \|\mathbf{u}\|_{\mathbf{PH}^2(\Omega)}. \quad \square \end{aligned} \tag{4.28}$$

4.2. Semi-discrete analysis

In this subsection, we present the error estimation for the semi-discrete scheme (3.4).

Theorem 4.2. *Assume that $\mathbf{u} \in W^{2,\infty}(0, L; \mathbf{PH}^2)$ is the exact solution of (1.1), and $\boldsymbol{\omega}_0 \in \mathbf{PH}^2(\Omega)$. Let $\mathbf{u}_h$ be the solution of semi-discrete scheme (3.4), then the following estimate holds for any time $t \in [0, L]$:*

$$|||\mathbf{u}(t) - \mathbf{u}_h(t)|||_h \lesssim (1+t)h \left(\|\boldsymbol{\omega}_0\|_{\mathbf{PH}^2} + \|\mathbf{u}\|_{W^{2,\infty}(0,L;\mathbf{PH}^2)} \right). \tag{4.29}$$

Proof. We decompose the error function $\mathbf{e}_h(t) = \mathbf{u}(t) - \mathbf{u}_h(t) = \boldsymbol{\xi}_h(t) + \boldsymbol{\eta}_h(t)$, where $\boldsymbol{\xi}_h(t) = \mathbf{u}(t) - \mathcal{R}_h\mathbf{u}(t)$ and $\boldsymbol{\eta}_h(t) = \mathcal{R}_h\mathbf{u}(t) - \mathbf{u}_h(t)$, where $\mathcal{R}_h\mathbf{u}$ is the elastic projection of $\mathbf{u}$. The bound for $\boldsymbol{\xi}_h(t)$ is a direct result from approximation property:

$$|||\boldsymbol{\xi}_h(t)|||_h \lesssim h\,\|\mathbf{u}(t)\|_{\mathbf{PH}^2} \lesssim h \left(\|\mathbf{u}_0\|_{\mathbf{PH}^2} + \int_0^t \|\mathbf{u}_t(s)\|_{\mathbf{PH}^2}\, ds \right) \lesssim h \left(\|\boldsymbol{\omega}_0\|_{\mathbf{PH}^2} + t\,\|\mathbf{u}_t\|_{L^\infty(0,L;\mathbf{PH}^2)} \right). \tag{4.30}$$

To bound $\boldsymbol{\eta}_h(t)$, we use (3.3a), (3.4a) and the definition of $\mathcal{R}_h\mathbf{u}$ to obtain

$$((\mathbf{u} - \mathbf{u}_h)_{tt}, \mathbf{v}_h) + a_h(\boldsymbol{\eta}_h(t), \mathbf{v}_h) = 0. \tag{4.31}$$

By the above decomposition we have

$$(\boldsymbol{\eta}_{h,tt}, \mathbf{v}_h) + a_h(\boldsymbol{\eta}_h(t), \mathbf{v}_h) = -(\boldsymbol{\xi}_{h,tt}, \mathbf{v}_h). \tag{4.32}$$

Choosing $\mathbf{v}_h = \boldsymbol{\eta}_{h,t}(t)$, the bi-linearity of $a_h(\cdot,\cdot)$ and $(\cdot,\cdot)$, and Cauchy-Schwarz inequality yield

$$\frac{d}{dt}(\|\boldsymbol{\eta}_{h,t}\|^2 + a_h(\boldsymbol{\eta}_h, \boldsymbol{\eta}_h)) \lesssim \|\boldsymbol{\xi}_{h,tt}\|\,\|\boldsymbol{\eta}_{h,t}\|. \tag{4.33}$$

This bound can be loosened as

$$\frac{d}{dt}\left(\|\boldsymbol{\eta}_{h,t}\|^2 + a_h(\boldsymbol{\eta}_h, \boldsymbol{\eta}_h) \right) \lesssim \|\boldsymbol{\xi}_{h,tt}\| \left(\|\boldsymbol{\eta}_{h,t}\| + \sqrt{a_h(\boldsymbol{\eta}_h, \boldsymbol{\eta}_h)} \right). \tag{4.34}$$

Then the above inequality leads to

$$\frac{d}{dt}\left(\left(\|\boldsymbol{\eta}_{h,t}\|^2 + a_h(\boldsymbol{\eta}_h,\boldsymbol{\eta}_h)\right)^{1/2}\right) \lesssim \|\boldsymbol{\xi}_{h,tt}\|. \tag{4.35}$$

Integrating (4.35) over $[0,t]$, we have

$$\left(\|\boldsymbol{\eta}_{h,t}\|^2 + a_h(\boldsymbol{\eta}_h,\boldsymbol{\eta}_h)\right)^{1/2} \lesssim \left(\|\boldsymbol{\eta}_{h,t}(0)\|^2 + a_h(\boldsymbol{\eta}_h(0),\boldsymbol{\eta}_h(0))\right)^{1/2} + \int_0^t \|\boldsymbol{\xi}_{h,tt}(s)\|\,ds. \tag{4.36}$$

Then by the continuity and coercivity of $a_h(\cdot,\cdot)$, we have

$$|||\boldsymbol{\eta}_h|||_h \lesssim \left(\|\boldsymbol{\eta}_{h,t}(0)\|^2 + |||\boldsymbol{\eta}_h(0)|||_h^2\right)^{1/2} + t\,\|\boldsymbol{\xi}_{h,tt}\|_{L^\infty(0,L;L^2)}. \tag{4.37}$$

Due to our choices of $\boldsymbol{\eta}_{h,t}(0)$ and $\boldsymbol{\eta}_h(0)$, the first term on the right hand side is zero. By the commutativity of $\mathcal{R}_h$ and the t derivative, (3.7b), we obtain

$$|||\boldsymbol{\eta}_h|||_h \lesssim th^2\,\|\mathbf{u}\|_{W^{2,\infty}(0,L;\mathbf{PH}^2)}. \tag{4.38}$$

Finally, we combine (4.30) and (4.38) to obtain (4.29). □

Remark 4.2. From (4.38), we can see that the elastic projection of initial condition is not the only choice. As long as the estimates of $\boldsymbol{\eta}_{h,t}(0)$ and $\boldsymbol{\eta}_h(0)$ have sufficient order of approximation, the above estimates would still hold. For example, we can take the interpolation $\mathbf{u}_h(0) = \mathcal{I}_h\boldsymbol{\omega}_0$ and $\mathbf{u}_{h,t}(0) = \mathcal{I}_h\boldsymbol{\omega}_1$. Then $|||\boldsymbol{\eta}_h(0)|||_h = |||\mathcal{R}_h\mathbf{u}(0) - \mathcal{I}_h\mathbf{u}(0)|||_h \lesssim |||\mathcal{R}_h\mathbf{u}(0) - \mathbf{u}(0)|||_h + |||\mathbf{u}(0) - \mathcal{I}_h\mathbf{u}(0)|||_h$, which has the desired approximating order h. Similar results hold for $\|\boldsymbol{\eta}_{h,t}(0)\|$.

We then derive the error estimates for the semi-discrete scheme in the semi-H^1 and the L^2 norms.

Theorem 4.3. *Assume that $\mathbf{u} \in W^{1,\infty}(0,L;\mathbf{PH}^2)$ is the exact solution of (1.1) and $\boldsymbol{\omega}_0$, $\boldsymbol{\omega}_1 \in \mathbf{PH}^2(\Omega)$. Let $\mathbf{u}_h$ be the solution of semi-discrete problem (3.4), then the following estimate holds for any time $t \in [0,L]$:*

$$\|\mathbf{u}(t) - \mathbf{u}_h(t)\|_{L^2(\Omega)} + h|\mathbf{u}(t) - \mathbf{u}_h(t)|_{H^1(\mathcal{T}_h)} \lesssim (1+t)h^2\left(\|\boldsymbol{\omega}_0\|_{\mathbf{PH}^2} + \|\boldsymbol{\omega}_1\|_{\mathbf{PH}^2} + \|\mathbf{u}\|_{W^{1,\infty}(0,L;\mathbf{PH}^2)}\right).$$

Proof. We use the decomposition of the error function again as follows

$$(\boldsymbol{\eta}_{h,tt},\mathbf{v}_h) + a_h(\boldsymbol{\eta}_h(t),\mathbf{v}_h) = -(\boldsymbol{\xi}_{h,tt},\mathbf{v}_h). \tag{4.39}$$

Integrating this equality from 0 to t we obtain

$$(\boldsymbol{\eta}_{h,t},\mathbf{v}_h) + a_h\left(\int_0^t \boldsymbol{\eta}_h(s)ds,\mathbf{v}_h\right) = -(\boldsymbol{\xi}_{h,t},\mathbf{v}_h) + (\boldsymbol{\eta}_{h,t}(0),\mathbf{v}_h) + (\boldsymbol{\xi}_{h,t}(0),\mathbf{v}_h). \tag{4.40}$$

Choosing $\mathbf{v}_h = \boldsymbol{\eta}_h$ and using the bi-linearity of $a_h(\cdot,\cdot)$, $(\cdot,\cdot)$ and Cauchy-Schwarz inequality, we have

$$\frac{d}{dt}\left(\|\boldsymbol{\eta}_h\|^2 + a_h\left(\int_0^t \boldsymbol{\eta}_h(s)ds, \int_0^t \boldsymbol{\eta}_h(s)ds\right)\right) \lesssim \|\boldsymbol{\xi}_{h,t}\|\,\|\boldsymbol{\eta}_h\| + \|\boldsymbol{\eta}_{h,t}(0)\|\,\|\boldsymbol{\eta}_h\| + \|\boldsymbol{\xi}_{h,t}(0)\|\,\|\boldsymbol{\eta}_h\|. \tag{4.41}$$

Note that $\boldsymbol{\eta}_{h,t}(0) = \mathbf{0}$, then (4.41) can be written as

$$\frac{d}{dt}\left(\|\boldsymbol{\eta}_h\|^2 + a_h\left(\int_0^t \boldsymbol{\eta}_h(s)ds, \int_0^t \boldsymbol{\eta}_h(s)ds\right)\right) \lesssim \left(\|\boldsymbol{\xi}_{h,t}\| + \|\boldsymbol{\xi}_{h,t}(0)\|\right)\|\boldsymbol{\eta}_h\|. \tag{4.42}$$

Similar to the proof of Theorem 4.2, we loose (4.42) as

$$\begin{aligned}&\frac{d}{dt}\left(\|\boldsymbol{\eta}_h\|^2 + a_h\left(\int_0^t \boldsymbol{\eta}_h(s)ds, \int_0^t \boldsymbol{\eta}_h(s)ds\right)\right)\\ &\lesssim \left(\|\boldsymbol{\xi}_{h,t}\| + \|\boldsymbol{\xi}_{h,t}(0)\|\right)\left(\|\boldsymbol{\eta}_h\| + \left(a_h\left(\int_0^t \boldsymbol{\eta}_h(s)ds, \int_0^t \boldsymbol{\eta}_h(s)ds\right)\right)^{1/2}\right).\end{aligned} \tag{4.43}$$

This leads to

$$\frac{d}{dt}\left(\|\boldsymbol{\eta}_h\|^2 + a_h\left(\int_0^t \boldsymbol{\eta}_h(s)ds, \int_0^t \boldsymbol{\eta}_h(s)ds\right)\right)^{1/2} \lesssim \left(\|\boldsymbol{\xi}_{h,t}\| + \|\boldsymbol{\xi}_{h,t}(0)\|\right). \tag{4.44}$$

Integrate (4.44) from 0 to t, we have

$$\left(\|\boldsymbol{\eta}_h\|^2 + a_h\left(\int_0^t \boldsymbol{\eta}_h(s)ds, \int_0^t \boldsymbol{\eta}_h(s)ds\right)\right)^{1/2} \lesssim \int_0^t \|\boldsymbol{\xi}_{h,t}(s)\|\,ds + \|\boldsymbol{\xi}_{h,t}(0)\|\,t. \tag{4.45}$$

Using the positivity $a_h(\cdot,\cdot)$ and the approximation property of $\mathcal{R}_h$, we have

$$\|\boldsymbol{\eta}_h\| \lesssim t\,\|\boldsymbol{\xi}_{h,t}\|_{L^\infty(0,L;L^2)} \lesssim th^2(\|\mathbf{u}\|_{W^{1,\infty}(0,L;\mathbf{PH}^2)} + \|\boldsymbol{\omega}_1\|_{\mathbf{PH}^2}). \tag{4.46}$$

Similarly with the energy norm, we have the estimate for $\boldsymbol{\xi}_h$

$$\|\boldsymbol{\xi}_h\| \lesssim h^2\,\|\mathbf{u}(t)\|_{\mathbf{PH}^2} \lesssim h^2\left(\|\mathbf{u}_0\|_{\mathbf{PH}^2} + \int_0^t \|\mathbf{u}_t(s)\|_{\mathbf{PH}^2}\,ds\right) \lesssim h^2\left(\|\boldsymbol{\omega}_0\|_{\mathbf{PH}^2} + t\,\|\mathbf{u}_t\|_{L^\infty(0,L;\mathbf{PH}^2)}\right). \tag{4.47}$$

Then we obtain the estimate in the L^2 norm using the triangle inequality. For the error bound in semi-H^1 norm, note that $\boldsymbol{\eta}_h \in \mathbf{S}_h$. Applying the inverse estimate in Theorem 4.1, we have $h\sum_{T\in\mathcal{T}_h}|\boldsymbol{\eta}_h|_{H^1(T)} \lesssim \|\boldsymbol{\eta}_h\|$. Then the semi-$H^1$ norm estimate is obtained by combining the above results with the approximation property of the elastic projection stated in Theorem 3.1. □

4.3. Fully discrete analysis

In this subsection, we provide the error analysis for the fully discrete scheme (3.10). We first derive the stability for our scheme. For simplicity, we let $\mathbf{f} = \mathbf{0}$ in the analysis below.

Theorem 4.4 *(Stability). The fully discrete scheme* (3.10) *is unconditionally stable and satisfies the following stability result for* $M \geq 1$*:*

$$\frac{\left\|\mathbf{u}_h^{M+1} - \mathbf{u}_h^M\right\|^2}{\tau^2} + \left|\!\left|\!\left|\mathbf{u}_h^{M+1/2}\right|\!\right|\!\right|_h^2 \lesssim \frac{\left\|\mathbf{u}_h^1 - \mathbf{u}_h^0\right\|^2}{\tau^2} + \left|\!\left|\!\left|\mathbf{u}_h^{1/2}\right|\!\right|\!\right|_h^2. \tag{4.48}$$

Proof. In (3.10), we let $\mathbf{v}_h = \mathbf{u}_h^{n+1} - \mathbf{u}_h^{n-1}$, then

$$\begin{aligned}&(\mathbf{u}_h^{n+1} - \mathbf{u}_h^n - (\mathbf{u}_h^n - \mathbf{u}_h^{n-1}), \mathbf{u}_h^{n+1} - \mathbf{u}_h^n + (\mathbf{u}_h^n - \mathbf{u}_h^{n-1}))\\ &+\frac{\tau^2}{4}a_h(\mathbf{u}_h^{n+1} + \mathbf{u}_h^n + \mathbf{u}_h^n + \mathbf{u}_h^{n-1}, \mathbf{u}_h^{n+1} + \mathbf{u}_h^n - (\mathbf{u}_h^n + \mathbf{u}_h^{n-1})) = 0.\end{aligned} \tag{4.49}$$

By the symmetry and bi-linearity of $(\cdot,\cdot)$ and $a_h(\cdot,\cdot)$ we have

$$\left\|\mathbf{u}_h^{n+1} - \mathbf{u}_h^n\right\|^2 - \left\|\mathbf{u}_h^n - \mathbf{u}_h^{n-1}\right\|^2 + \tau^2 a_h(\mathbf{u}_h^{n+1/2}, \mathbf{u}_h^{n+1/2}) - \tau^2 a_h(\mathbf{u}_h^{n-1/2}, \mathbf{u}_h^{n-1/2}) = 0. \tag{4.50}$$

The following recursive relation holds

$$\left\|\mathbf{u}_h^{n+1} - \mathbf{u}_h^n\right\|^2 + \tau^2 a_h(\mathbf{u}_h^{n+1/2}, \mathbf{u}_h^{n+1/2}) = \left\|\mathbf{u}_h^n - \mathbf{u}_h^{n-1}\right\|^2 + \tau^2 a_h(\mathbf{u}_h^{n-1/2}, \mathbf{u}_h^{n-1/2}). \tag{4.51}$$

Summing (4.51)over $n = 1, 2, \cdots, M$, we have

$$\left\|\mathbf{u}_h^{M+1} - \mathbf{u}_h^M\right\|^2 + \tau^2 a_h(\mathbf{u}_h^{M+1/2}, \mathbf{u}_h^{M+1/2}) = \left\|\mathbf{u}_h^1 - \mathbf{u}_h^0\right\|^2 + \tau^2 a_h(\mathbf{u}_h^{1/2}, \mathbf{u}_h^{1/2}). \tag{4.52}$$

By the continuity and coercivity of $a_h(\cdot,\cdot)$, we obtain

$$\left\|\mathbf{u}_h^{M+1} - \mathbf{u}_h^M\right\|^2 + \tau^2\left|\!\left|\!\left|\mathbf{u}_h^{M+1/2}\right|\!\right|\!\right|_h^2 \lesssim \left\|\mathbf{u}_h^1 - \mathbf{u}_h^0\right\|^2 + \tau^2\left|\!\left|\!\left|\mathbf{u}_h^{1/2}\right|\!\right|\!\right|_h^2. \tag{4.53}$$

This completes the proof of the stability. □

Now we derive an error estimate for the fully discrete scheme. Similar to semi-discrete analysis, we decompose the error $\mathbf{e}_h^n = \mathbf{u}^n - \mathbf{u}_h^n$ into $\boldsymbol{\xi}_h^n + \boldsymbol{\eta}_h^n$. In the following lemma, we first estimate the one-step approximation $\mathbf{u}_h^1$ and use it to discuss the impact of the approximations of initial conditions.

Lemma 4.5. *Assume that* $\mathbf{u}$ *is the exact solution of* (1.1) *and satisfies* $\mathbf{u}_{ttt} \in \mathbf{L}^\infty(0, L; \mathbf{PH}^2(\Omega))$*. Then the following estimate for* $\mathbf{u}_h^1$ *holds*

$$\left\|\boldsymbol{\eta}_h^1\right\| \lesssim \left|\!\left|\!\left|\boldsymbol{\eta}_h^1\right|\!\right|\!\right|_h \lesssim \tau^3\|\mathbf{u}_{ttt}\|_{\mathbf{L}^\infty(0,L;\mathbf{PH}^2(\Omega))}. \tag{4.54}$$

Proof. By the coercivity of $a_h(\cdot,\cdot)$, the definition of $\mathcal{R}_h$ and $\mathbf{u}_h^1$, we have:

$$\left|\!\left|\!\left|\boldsymbol{\eta}_h^1\right|\!\right|\!\right|_h^2 \lesssim a_h(\boldsymbol{\eta}_h^1, \boldsymbol{\eta}_h^1) = a_h(\mathcal{R}_h\mathbf{u}^1 - \mathbf{u}_h^1, \boldsymbol{\eta}_h^1) = a_h(\mathcal{R}_h\mathbf{u}^1 - \mathcal{R}_h\mathbf{u}^{1,*}, \boldsymbol{\eta}_h^1) = a_h(\mathbf{u}^1 - \mathbf{u}^{1,*}, \boldsymbol{\eta}_h^1). \tag{4.55}$$

Recall that $\mathbf{u}^{1,*} = \boldsymbol{\omega}_0 + \tau\boldsymbol{\omega}_1 + \frac{\tau^2}{2}\boldsymbol{u}_{tt}(\mathbf{x}, 0)$ is an approximation of $\mathbf{u}_1$. Using the continuity of $a_h(\cdot,\cdot)$, we have

$$a_h(\mathbf{u}^1 - \mathbf{u}^{1,*}, \boldsymbol{\eta}_h^1) \lesssim \left|\!\left|\!\left|\mathbf{u}^1 - \mathbf{u}^{1,*}\right|\!\right|\!\right|_h \left|\!\left|\!\left|\boldsymbol{\eta}_h^1\right|\!\right|\!\right|_h.$$

Thus,

$$\left|\!\left|\!\left|\boldsymbol{\eta}_h^1\right|\!\right|\!\right|_h \lesssim \left|\!\left|\!\left|\mathbf{u}^1 - \mathbf{u}^{1,*}\right|\!\right|\!\right|_h. \tag{4.56}$$

Using Lemma 4.4 to bound the right hand side of the above inequality, we have

$$\begin{aligned}\left|\left|\left|\mathbf{u}^1-\mathbf{u}^{1,*}\right|\right|\right|_h^2 &= \sum_{T\in\mathcal{T}_h}\int_T 2\mu\|\epsilon(\mathbf{u}^1-\mathbf{u}^{1,*})\|^2 d\mathbf{x}+\sum_{T\in\mathcal{T}_h}\int_T \lambda\|\nabla\cdot(\mathbf{u}^1-\mathbf{u}^{1,*})\|^2 d\mathbf{x}+\sum_{e\in\mathcal{E}_h^i}\rho^{-1}\int_e \|h^{1/2}\left\{\left\{\sigma(\mathbf{u}^1-\mathbf{u}^{1,*})\mathbf{n}_e\right\}\right\}\|^2 ds \\ &\lesssim \|\mathbf{u}^1-\mathbf{u}^{1,*}\|^2_{\mathbf{PH}^2(\Omega)}.\end{aligned} \tag{4.57}$$

Then we obtain the estimate using Taylor Theorem:

$$\begin{aligned}\left|\left|\left|\boldsymbol{\eta}_h^1\right|\right|\right|_h \lesssim \left|\left|\left|\mathbf{u}^1-\mathbf{u}^{1,*}\right|\right|\right|_h &\lesssim \|\mathbf{u}^1-\mathbf{u}^{1,*}\|_{\mathbf{PH}^2(\Omega)} = \left\|\int_0^\tau \mathbf{u}_{ttt}^1(s)\frac{(s-\tau)^2}{2}ds\right\|_{\mathbf{PH}^2(\Omega)} \\ &\lesssim \tau^3\|\mathbf{u}_{ttt}\|_{\mathbf{L}^\infty(0,L;\mathbf{PH}^2(\Omega))}.\end{aligned} \tag{4.58}$$

The estimate for $\|\cdot\|_{L^2}$ holds thanks to Lemma 4.3 and $\boldsymbol{\eta}_h^1\in\mathbf{S}_h(\Omega)$. □

Lemma 4.6. *Assume that $\mathbf{u}(\cdot,t)\in\mathbf{PH}^2(\Omega)$ is the exact solution of (1.1) and satisfies the regularity condition $\mathbf{u}_{tttt}\in L^\infty(0,L;\mathbf{PH}^2)$. Then the following estimate holds for $0\le n\le M-1$:*

$$\left\|\mathbf{u}_{tt}^{n,1/4}-\partial_{tt}\mathbf{u}^n\right\| \lesssim \tau^2\left\|\mathbf{u}_{tttt}\right\|_{L^\infty(0,L;\mathbf{PH}^2)}. \tag{4.59}$$

Proof. We can write $\left\|\mathbf{u}_{tt}^{n,1/4}-\partial_{tt}\mathbf{u}^n\right\|$ as follows

$$\left\|\mathbf{u}_{tt}^{n,1/4}-\partial_{tt}\mathbf{u}^n\right\|^2 = \left\|\frac{\mathbf{u}_{tt}^{n+1}+2\mathbf{u}_{tt}^n+\mathbf{u}_{tt}^{n-1}}{4}-\frac{\mathbf{u}^{n+1}-2\mathbf{u}^n+\mathbf{u}^{n-1}}{\tau^2}\right\|^2. \tag{4.60}$$

The first term can be expanded using Taylor Theorem

$$\frac{\mathbf{u}_{tt}^{n+1}+2\mathbf{u}_{tt}^n+2\mathbf{u}_{tt}^{n-1}}{4} = \mathbf{u}_{tt}^n+\int_{t^n}^{t^{n+1}}\mathbf{u}_{tttt}(s)(t^{n+1}-s)ds+\int_{t^n}^{t^{n-1}}\mathbf{u}_{tttt}(s)(t^{n-1}-s)ds. \tag{4.61}$$

Similarly, we expand the second term into

$$\frac{\mathbf{u}^{n+1}-2\mathbf{u}^n+\mathbf{u}^{n-1}}{\tau^2} = \mathbf{u}_{tt}^n+\frac{1}{6\tau^2}\int_{t^n}^{t^{n+1}}\mathbf{u}_{tttt}(s)(t^{n+1}-s)^3ds+\frac{1}{6\tau^2}\int_{t^n}^{t^{n-1}}\mathbf{u}_{tttt}(s)(t^{n-1}-s)^3ds. \tag{4.62}$$

We bound the remaining terms separately using Cauchy-Schwarz inequality and Fubini's Theorem:

$$\begin{aligned}&\left\|\int_{t^n}^{t^{n+1}}\mathbf{u}_{tttt}(s)(t^{n+1}-s)ds+\int_{t^n}^{t^{n-1}}\mathbf{u}_{tttt}(s)(t^{n-1}-s)ds\right\|^2 \\ \lesssim&\tau^3\left\|\left(\int_{t^n}^{t^{n+1}}|\mathbf{u}_{tttt}(s)|^2ds\right)^{1/2}+\left(\int_{t^n}^{t^{n-1}}|\mathbf{u}_{tttt}(s)|^2ds\right)^{1/2}\right\|^2 \\ \lesssim&\tau^3\int_{t^{n-1}}^{t^{n+1}}\left\|\mathbf{u}_{tttt}(s)\right\|^2ds\lesssim\tau^4\left\|\mathbf{u}_{tttt}\right\|^2_{L^\infty(0,L;\mathbf{PH}^2)}.\end{aligned} \tag{4.63}$$

Similarly for the other two terms, we have

$$\begin{aligned}&\left\|\frac{1}{\tau^2}\int_{t^n}^{t^{n+1}}\mathbf{u}_{tttt}(s)(t^{n+1}-s)^3ds+\frac{1}{\tau^2}\int_{t^n}^{t^{n-1}}\mathbf{u}_{tttt}(s)(t^{n-1}-s)^3ds\right\|^2 \\ \lesssim&\tau^3\left\|\left(\int_{t^n}^{t^{n+1}}|\mathbf{u}_{tttt}(s)|^2ds\right)^{1/2}+\left(\int_{t^n}^{t^{n-1}}|\mathbf{u}_{tttt}(s)|^2ds\right)^{1/2}\right\|^2 \\ \lesssim&\tau^3\int_{t^{n-1}}^{t^{n+1}}\left\|\mathbf{u}_{tttt}(s)\right\|^2ds\lesssim\tau^4\left\|\mathbf{u}_{tttt}\right\|^2_{L^\infty(0,L;\mathbf{PH}^2)}.\end{aligned} \tag{4.64}$$

□

Now we are ready to derive the error estimates in energy norm for the fully discrete scheme (3.10).

Theorem 4.5. *Assume that $\mathbf{u}\in W^{4,\infty}(0,L;\mathbf{PH}^2)$ is the exact solution of (1.1), and $\mathbf{u}_h$ is the solution of fully discrete problem (3.10). Then the following estimate holds for $0\le n\le M-1$:*

$$\left|\left|\left|\mathbf{u}^{n+1/2}-\mathbf{u}_h^{n+1/2}\right|\right|\right|_h \lesssim (L+1)\left(\tau^2+h\right)\|\mathbf{u}\|_{W^{4,\infty}(0,L;\mathbf{PH}^2)}. \tag{4.65}$$

Proof. We evaluate the weak form (3.3a) at t^{n-1}, t^n, t^{n+1}. By the bi-linearity of $a_h(\cdot,\cdot)$ and $(\cdot,\cdot)$, we have for every $\mathbf{v}_h\in\mathbf{S}_h$:

$$(\mathbf{u}_{tt}^{n,1/4},\mathbf{v}_h)+a_h(\mathbf{u}^{n,1/4},\mathbf{v}_h)=L_{\mathbf{f}^{n,1/4}}(\mathbf{v}_h). \tag{4.66}$$

Combining (4.66) and (3.10a), we have

$$(\partial_{tt}\mathbf{u}_h^n-\mathbf{u}_{tt}^{n,1/4},\mathbf{v}_h)+a_h((\mathbf{u}_h-\mathbf{u})^{n,1/4},\mathbf{v}_h)=0. \tag{4.67}$$

With the definition of $\mathcal{R}_h$, (4.67) can be decomposed into

$$(\partial_{tt}\boldsymbol{\eta}_h^n,\mathbf{v}_h)+a_h(\boldsymbol{\eta}_h^{n,1/4},\mathbf{v}_h)=-(\partial_{tt}\boldsymbol{\xi}_h^n,\mathbf{v}_h)-(\mathbf{u}_{tt}^{n,1/4}-\partial_{tt}\mathbf{u}^n,\mathbf{v}_h). \tag{4.68}$$

Then we take $\mathbf{v}_h=\partial_t\boldsymbol{\eta}_h^n$, which can be written as

$$\partial_t\boldsymbol{\eta}_h^n=\frac{\boldsymbol{\eta}_h^{n+1}-\boldsymbol{\eta}_h^{n-1}}{2\tau}=\frac{\boldsymbol{\eta}_h^{n+1/2}-\boldsymbol{\eta}_h^{n-1/2}}{\tau}=\frac{\partial_t\boldsymbol{\eta}_h^{n+1/2}+\partial_t\boldsymbol{\eta}_h^{n-1/2}}{2}. \tag{4.69}$$

Also for any vector function $\mathbf{w}$, we have

$$\partial_{tt}\mathbf{w}^n=\frac{\partial_t\mathbf{w}^{n+1/2}-\partial_t\mathbf{w}^{n-1/2}}{\tau},\quad \mathbf{w}^{n,1/4}=\frac{\mathbf{w}^{n+1/2}+\mathbf{w}^{n-1/2}}{2}. \tag{4.70}$$

By Cauchy-Schwarz inequality, we obtain the following from (4.68):

$$\begin{aligned}&\frac{1}{2\tau}(\partial_t\boldsymbol{\eta}_h^{n+1/2}-\partial_t\boldsymbol{\eta}_h^{n-1/2},\partial_t\boldsymbol{\eta}_h^{n+1/2}+\partial_t\boldsymbol{\eta}_h^{n-1/2})+\frac{1}{2\tau}a_h(\boldsymbol{\eta}_h^{n+1/2}+\boldsymbol{\eta}_h^{n-1/2},\boldsymbol{\eta}_h^{n+1/2}-\boldsymbol{\eta}_h^{n-1/2})\\ \le&\frac{1}{2}\left(\left\|\partial_{tt}\boldsymbol{\xi}_h^n\right\|+\left\|\mathbf{u}_{tt}^{n,1/4}-\partial_{tt}\mathbf{u}^n\right\|\right)\left(\left\|\partial_t\boldsymbol{\eta}_h^{n+1/2}\right\|+\left\|\partial_t\boldsymbol{\eta}_h^{n-1/2}\right\|\right).\end{aligned} \tag{4.71}$$

By the bilinearity and the symmetry of $a_h(\cdot,\cdot)$ and $(\cdot,\cdot)$, we have:

$$\begin{aligned}&\left(\left\|\partial_t\boldsymbol{\eta}_h^{n+1/2}\right\|^2-\left\|\partial_t\boldsymbol{\eta}_h^{n-1/2}\right\|^2\right)+a_h(\boldsymbol{\eta}_h^{n+1/2},\boldsymbol{\eta}_h^{n+1/2})-a_h(\boldsymbol{\eta}_h^{n-1/2},\boldsymbol{\eta}_h^{n-1/2})\\ \le&\tau\left(\left\|\partial_{tt}\boldsymbol{\xi}_h^n\right\|+\left\|\mathbf{u}_{tt}^{n,1/4}-\partial_{tt}\mathbf{u}^n\right\|\right)\left(\left\|\partial_t\boldsymbol{\eta}_h^{n+1/2}\right\|+\left\|\partial_t\boldsymbol{\eta}_h^{n-1/2}\right\|\right).\end{aligned} \tag{4.72}$$

Denote $Q_1=\left\|\partial_{tt}\boldsymbol{\xi}_h^n\right\|$ and $Q_2=\left\|\mathbf{u}_{tt}^{n,1/4}-\partial_{tt}\mathbf{u}^n\right\|$. For Q_1 we have the following estimate using Taylor expansion

$$\begin{aligned}\left\|\partial_{tt}\boldsymbol{\xi}_h^n\right\|&=\left\|\frac{\boldsymbol{\xi}_h^{n-1}-2\boldsymbol{\xi}_h^n+\boldsymbol{\xi}_h^{n+1}}{\tau^2}\right\|\\ &=\left\|\frac{1}{\tau^2}\left(\int_{t^n}^{t^{n+1}}\boldsymbol{\xi}_{tt,h}(s)(t^{n+1}-s)ds+\int_{t^n}^{t^{n-1}}\boldsymbol{\xi}_{tt,h}(s)(t^{n-1}-s)ds\right)\right\|\\ &\lesssim\left\|\frac{1}{\tau^{1/2}}\left[\left(\int_{t^n}^{t^{n+1}}|\boldsymbol{\xi}_{tt,h}(s)|^2ds\right)^{1/2}+\left(\int_{t^{n-1}}^{t^n}|\boldsymbol{\xi}_{tt,h}(s)|^2ds\right)^{1/2}\right]\right\|\\ &\lesssim\left(\frac{1}{\tau}\int_{t^{n-1}}^{t^{n+1}}\left\|\boldsymbol{\xi}_{tt,h}(s)\right\|^2ds\right)^{1/2}.\end{aligned} \tag{4.73}$$

The approximation capability of $\mathcal{R}_h\mathbf{u}_{tt}$ yields

$$Q_1\lesssim\left\|\boldsymbol{\xi}_{tt,h}\right\|_{L^\infty(0,L;L^2)}\lesssim h^2\left\|\mathbf{u}_{tt}\right\|_{L^\infty(0,L;\mathbf{PH}^2)}. \tag{4.74}$$

We next bound Q_2 using Lemma 4.6:

$$Q_2\lesssim\tau^2\left\|\mathbf{u}_{tttt}\right\|_{L^\infty(0,L;\mathbf{PH}^2)}. \tag{4.75}$$

Combining the above estimates and summing (4.72) from 1 to M, we get

$$\left\|\partial_t\boldsymbol{\eta}_h^{M+1/2}\right\|^2+\left|\left|\left|\boldsymbol{\eta}_h^{M+1/2}\right|\right|\right|_h^2\lesssim\tau\left(\tau^2+h^2\right)\|\mathbf{u}\|_{W^{4,\infty}(0,L;\mathbf{PH}^2)}\left(\sum_{n=0}^{M}\left\|\partial_t\boldsymbol{\eta}_h^{n+1/2}\right\|\right)+\left\|\partial_t\boldsymbol{\eta}_h^{1/2}\right\|^2+\left|\left|\left|\boldsymbol{\eta}_h^{1/2}\right|\right|\right|_h^2. \tag{4.76}$$

Denote $Q_3=\left\|\partial_t\boldsymbol{\eta}_h^{1/2}\right\|^2$ and $Q_4=\left|\left|\left|\boldsymbol{\eta}_h^{1/2}\right|\right|\right|_h^2$. Then by Lemma 4.5 we obtain

$$Q_3=\frac{1}{\tau^2}\left\|\boldsymbol{\eta}_h^1-\boldsymbol{\eta}_h^0\right\|^2\le\frac{1}{\tau^2}\left(\left\|\boldsymbol{\eta}_h^1\right\|^2+\left\|\boldsymbol{\eta}_h^0\right\|^2\right)\lesssim\tau^4\left\|\mathbf{u}_{ttt}\right\|^2_{\mathbf{L}^\infty(0,T;\mathbf{PH}^2(\Omega))}, \tag{4.77}$$

$$Q_4=\frac{1}{4}\left|\left|\left|\boldsymbol{\eta}_h^1+\boldsymbol{\eta}_h^0\right|\right|\right|_h^2\le\frac{1}{4}\left(\left|\left|\left|\boldsymbol{\eta}_h^1\right|\right|\right|_h^2+\left|\left|\left|\boldsymbol{\eta}_h^0\right|\right|\right|_h^2\right)\lesssim\tau^6\left\|\mathbf{u}_{ttt}\right\|^2_{\mathbf{L}^\infty(0,T;\mathbf{PH}^2(\Omega))}. \tag{4.78}$$

Here we used $\boldsymbol{\eta}_h^0 = \mathbf{0}$, similar to semi-discrete analysis. We further denote the total energy error $\mathcal{E}_h^n$:

$$\mathcal{E}_h^n = \left\| \partial_t \boldsymbol{\eta}_h^{n+1/2} \right\| + \left\| \left\| \boldsymbol{\eta}_h^{n+1/2} \right\| \right\|_h. \tag{4.79}$$

With $\gamma = \left(\tau^2 + h^2\right) \|\mathbf{u}\|_{W^{4,\infty}(0,L;\mathbf{PH}^2)}$, one can obtain from (4.76):

$$(\mathcal{E}_h^M)^2 \lesssim \tau\gamma \sum_{n=0}^{M} \mathcal{E}_h^n + \gamma^2. \tag{4.80}$$

By an analogous mathematical induction procedure as Theorem 5.3 of [20], we obtain for $n \le M$:

$$\mathcal{E}_h^n \lesssim n\tau\gamma + \gamma. \tag{4.81}$$

In summary, we have the following estimate:

$$\left\| \partial_t \boldsymbol{\eta}_h^{M+1/2} \right\| + \left\| \left\| \boldsymbol{\eta}_h^{M+1/2} \right\| \right\|_h \lesssim (L+1)\left(\tau^2 + h^2\right) \|\mathbf{u}\|_{W^{4,\infty}(0,L;\mathbf{PH}^2)}. \tag{4.82}$$

With the approximation capability of operator $\mathcal{R}_h$, we have:

$$\left\| \left\| \boldsymbol{\xi}_h^{M+1/2} \right\| \right\|_h^2 \lesssim h^2 \|\mathbf{u}\|^2_{\mathbf{L}^\infty(0,L;\mathbf{PH}^2(\Omega))}. \tag{4.83}$$

Then by triangle inequality, we obtain

$$\left\| \left\| \mathbf{u}^{M+1/2} - \mathbf{u}_h^{M+1/2} \right\| \right\|_h \le \left\| \left\| \boldsymbol{\eta}_h^{M+1/2} \right\| \right\|_h + \left\| \left\| \boldsymbol{\xi}_h^{M+1/2} \right\| \right\|_h \lesssim (L+1)\left(\tau^2 + h\right) \|\mathbf{u}\|_{W^{4,\infty}(0,L;\mathbf{PH}^2)}. \quad \square \tag{4.84}$$

Remark 4.3. The analysis of the fully discrete scheme depends on the bound for $\boldsymbol{\eta}_h^0$ and $\boldsymbol{\eta}_h^1$ which depends on the choice of initial conditions. For $\boldsymbol{\eta}_h^0$, as mentioned in the Remark 4.2, we used the elastic projection to eliminate this error. However, similar to the semi-discrete scheme, any approximations that have appropriate error bounds also work. For $\boldsymbol{\eta}_h^1$, we notice from Lemma 4.5 that it depends on $\mathbf{u}^{1,*}$, the approximation of $\mathbf{u}^1$. Here we used a third order Taylor approximation to guarantee the convergence order. Again, any approximations that have appropriate error bounds could be taken.

Finally we derive the error estimate of the fully discrete scheme (3.10) in the semi-H^1 and the L^2 norm.

Theorem 4.6. *Let $\mathbf{u} \in W^{4,\infty}(0, L; \mathbf{PH}^2)$ be the exact solution of (1.1). Let $\mathbf{u}_h^n$, $n = 1, 2, \cdots, M$ be the solution of the fully discrete scheme (3.10). Then we have the following error bound: for $n = 0, 1, 2, \cdots, M$,*

$$\left\| \mathbf{u}_h^n - \mathbf{u}^n \right\|_{L^2(\Omega)} + h|\mathbf{u}_h^n - \mathbf{u}^n|_{H^1(\mathcal{T}_h)} \lesssim (L+1)\left(\tau^2 + h^2\right) \|\mathbf{u}\|_{W^{4,\infty}(0,L;\mathbf{PH}^2)}. \tag{4.85}$$

Proof. We first use Theorem 4.5 to obtain for $n = 0, 1, 2, \cdots, M-1$:

$$\left\| \boldsymbol{\eta}^{n+1} - \boldsymbol{\eta}^n \right\| = \tau \left\| \frac{\boldsymbol{\eta}^{n+1} - \boldsymbol{\eta}^n}{\tau} \right\| = \tau \left\| \partial_t \boldsymbol{\eta}^{n+1/2} \right\| \lesssim (L+1)\left(\tau^2 + h^2\right) \tau \|\mathbf{u}\|_{W^{4,\infty}(0,L;\mathbf{PH}^2)}. \tag{4.86}$$

Using Theorem 4.5 again and Lemma 4.3, we have for $n = 0, 1, 2, \cdots, M-1$:

$$\left\| \boldsymbol{\eta}^{n+1} + \boldsymbol{\eta}^n \right\| = 2 \left\| \boldsymbol{\eta}^{n+1/2} \right\| \lesssim \left\| \left\| \boldsymbol{\eta}^{n+1/2} \right\| \right\|_h \lesssim (L+1)\left(\tau^2 + h^2\right) \|\mathbf{u}\|_{W^{4,\infty}(0,L;\mathbf{PH}^2)}. \tag{4.87}$$

Applying the triangle inequality for $\left\| \boldsymbol{\eta}^{n+1} \right\|_{L^2(\Omega)}$ and $\|\boldsymbol{\eta}^n\|_{L^2(\Omega)}$, we obtain for $0 \le n \le M$:

$$\|\boldsymbol{\eta}^n\| \lesssim (L+1)\left(\tau^2 + h^2\right) \|\mathbf{u}\|_{W^{4,\infty}(0,L;\mathbf{PH}^2)}. \tag{4.88}$$

Finally, combining the above estimate with the approximation property of $\mathcal{R}_h$, we have

$$\left\| \mathbf{u}_h^n - \mathbf{u}^n \right\|_{L^2(\Omega)} \le \|\boldsymbol{\eta}^n\| + \|\boldsymbol{\xi}^n\| \lesssim (L+1)\left(\tau^2 + h^2\right) \|\mathbf{u}\|_{W^{4,\infty}(0,L;\mathbf{PH}^2)}. \tag{4.89}$$

This holds for $n = 0, 1, 2, ..., M$. The estimate for semi-H^1 norm is similar to the counterpart of Theorem 4.3. $\square$

5. Numerical experiments

In this section, we test the scheme with several numerical examples to validate the theoretical results. For all testing examples, we set the computational domain $\Omega = [-1, 1] \times [-1, 1]$. We use the $N \times N$ rectangular meshes with mesh size $h = 2/N$ and the bilinear IFE functions for approximations. The penalty parameter ρ is set to be 200 in the partially penalized IFE scheme (3.10).

Example 1 *(Accuracy test for an elliptical interface).* In this example, we consider an elastic plate consisting of two materials with an elliptical interface defined by $\Gamma = \{(x, y) \in \Omega : (x - x_0)^2 + k^2(y - y_0)^2 = r_0^2\}$. The domain Ω is separated by this interface into subdomains: $\Omega^+ = \{(x, y) \in \Omega : (x - x_0)^2 + k^2(y - y_0)^2 > r_0^2\}$ and $\Omega^- = \{(x, y) \in \Omega : (x - x_0)^2 + k^2(y - y_0)^2 < r_0^2\}$. The exact solution $\mathbf{u}(x, y, t) = (u^1(x, y, t), u^2(x, y, t))$ is given by:

$$u^1(x, y, t) = u^2(x, y, t) = \begin{cases} ((x - x_0)^2 + k^2(y - y_0)^2 - r_0^2)e^{-t}/\lambda^-, & \text{on } \Omega^-, t \in [0, L], \\ ((x - x_0)^2 + k^2(y - y_0)^2 - r_0^2)e^{-t}/\lambda^+, & \text{on } \Omega^+, t \in [0, L]. \end{cases} \tag{5.1}$$

Table 1
Errors of IFE solution u_h^1 in Example 1 at the ending time $t = 1$.

N	$\|u_h^1 - u^1\|_{L^\infty}$	order	$\|u_h^1 - u^1\|_{L^2}$	order	$\|u_h^1 - u^1\|_{H^1}$	order
10	6.0729×10^{-3}		1.5931×10^{-3}		2.6490×10^{-2}	
20	1.4951×10^{-3}	2.02	3.1828×10^{-4}	2.32	1.0079×10^{-2}	1.39
40	5.5554×10^{-4}	1.43	8.7658×10^{-5}	1.86	4.4691×10^{-3}	1.17
80	1.6197×10^{-4}	1.78	2.2762×10^{-5}	1.95	1.9995×10^{-3}	1.16
160	3.9072×10^{-5}	2.05	5.7313×10^{-6}	1.99	8.3509×10^{-4}	1.26
320	1.0734×10^{-5}	1.86	1.4442×10^{-6}	1.99	3.9268×10^{-4}	1.09
640	2.6959×10^{-6}	1.99	3.6185×10^{-7}	2.00	1.8569×10^{-4}	1.08

Table 2
Errors of IFE solution u_h^2 in Example 1 at the ending time $t = 1$.

N	$\|u_h^2 - u^2\|_{L^\infty}$	order	$\|u_h^2 - u^2\|_{L^2}$	order	$\|u_h^2 - u^2\|_{H^1}$	order
10	6.0982×10^{-3}		1.4027×10^{-3}		2.6297×10^{-2}	
20	1.6623×10^{-3}	1.88	3.1218×10^{-4}	2.17	1.0013×10^{-2}	1.39
40	4.4028×10^{-4}	1.92	1.0754×10^{-4}	1.54	4.5320×10^{-3}	1.14
80	1.4515×10^{-4}	1.60	2.8036×10^{-5}	1.94	1.9849×10^{-3}	1.19
160	4.2339×10^{-5}	1.78	7.0923×10^{-6}	1.98	8.3318×10^{-4}	1.25
320	1.0162×10^{-5}	2.06	1.7317×10^{-6}	2.03	3.8926×10^{-4}	1.10
640	2.4121×10^{-6}	2.07	4.2785×10^{-7}	2.02	1.8568×10^{-4}	1.07

The Lamé parameters are chosen to be $\lambda^+ = 100$, $\lambda^- = 10$, $\mu^+ = 10$ and $\mu^- = 1$. The parameters in the exact solution (5.1) are $x_0 = 0.2$, $y_0 = 0$, $k = 2.5$, and $r_0 = \pi/6.28$.

We set the time step size $\tau = h$ in our computation. In Tables 1 and 2, we list the errors of IFE solutions and the convergence rates for u_h^1 and u_h^2, respectively. Here, the L^∞ norm is computed as the maximum of the error among all finite element nodes. The contour plot for numerical solutions of Example 1 is shown in the left plot of Fig. 6.

Example 2 *(Accuracy for more complicated interface shapes).* In this example, we consider a more complicated star-shape interface. The level-set function of the interface is

$$\phi(x, y) = (x^2 + y^2)[1 + 0.6\sin(6\arctan(y/x))] - (\pi/6.28)^4,$$

which splits the whole domain Ω into two sub-domains $\Omega^+ = \{(x, y) \in \Omega : \phi(x, y) > 0\}$ and $\Omega^- = \{(x, y) \in \Omega : \phi(x, y) < 0\}$. We set the exact solution for this example to be

$$\mathbf{u}(x, y, t) = \begin{cases} \begin{pmatrix} u_1^-(x, y, t) \\ u_2^-(x, y, t) \end{pmatrix} = \begin{pmatrix} \frac{\phi(x,y)}{\lambda^-}\sin(t) \\ \frac{\phi(x,y)}{\lambda^-}\sin(t) \end{pmatrix}, & \text{on } \Omega^-, t \in [0, L] \\ \begin{pmatrix} u_1^+(x, y, t) \\ u_2^+(x, y, t) \end{pmatrix} = \begin{pmatrix} \frac{\phi(x,y)}{\lambda^+}\sin(t) \\ \frac{\phi(x,y)}{\lambda^+}\sin(t) \end{pmatrix}, & \text{on } \Omega^+, t \in [0, L] \end{cases} \tag{5.2}$$

where the Lamé parameters are chosen to be $\lambda^+ = 20$, $\lambda^- = 1$, $\mu^+ = 200$ and $\mu^- = 10$.

We set the time step size to be $\tau = h$. Errors at the final time $t = 1$ for u_1 and u_2 are reported in Tables 3 and 4, respectively. Optimal convergence rates for L^2 and semi-H^1 norms are observed which validate our theoretical results. Additionally, we also computed the error in L^∞ norm, which measures the largest difference of the numerical solution and the exact solution among all mesh points $\mathcal{N}_h$. The order of convergence is close to second order, which is considered optimal given the polynomial degree of the finite element spaces. The contour plot for numerical solutions of Example 2 is shown in the right plot of Fig. 6.

Example 3 *(Long-time behavior).* In this example, we investigate the long time behavior of our numerical scheme. In our analysis for the semi and fully discrete formulations, we obtain a bound of the numerical errors which is linear in time L. This means the numerical errors will grow at most linearly proportional to L. This conclusion is consistent to related studies of elastic wave problems using a Local Discontinuous Galerkin (LDG) method, such as [20]. In the following numerical example, we aim to explore the numerical behavior as the final time L increases dramatically. We consider a line interface $\Gamma = \{(x, y) \in \Omega : x + y - c = 0\}$. The subdomains are defined to be $\Omega^+ = \{(x, y) \in \Omega : x + y - c > 0\}$ and $\Omega^- = \{(x, y) \in \Omega : x + y - c < 0\}$. The exact solution $\mathbf{u}(x, y, t) = (u^1(x, y, t), u^2(x, y, t))$ is given by:

$$\mathbf{u}(x, y, t) = \begin{cases} \begin{pmatrix} (x + y - c)\sin(2\pi t + 1)/\lambda^- \\ [x^2 - (y - c)^2]\sin(2\pi t + 1)/\lambda^- \end{pmatrix}, & \text{on } \Omega^-, t \in [0, L], \\ \begin{pmatrix} (x + y - c)\sin(2\pi t + 1)/\lambda^+ \\ [x^2 - (y - c)^2]\sin(2\pi t + 1)/\lambda^+ \end{pmatrix}, & \text{on } \Omega^+, t \in [0, L]. \end{cases} \tag{5.3}$$

The Lamé parameters are taken as $\lambda^+ = 100$, $\mu^+ = 10$, $\lambda^- = 10$, $\mu^- = 1$, and the constant $c = 1.2$.

In our experiment, we let the mesh size $N = 40$, while the time step $\tau = h/16$. In Fig. 7, we report the L^2, L^∞ and semi-H^1 error norms of u_h^1 and u_h^2 against time up to $L = 5000$, which we consider to be a significantly long test interval for observation. In our tests, we find the errors of u_h^1

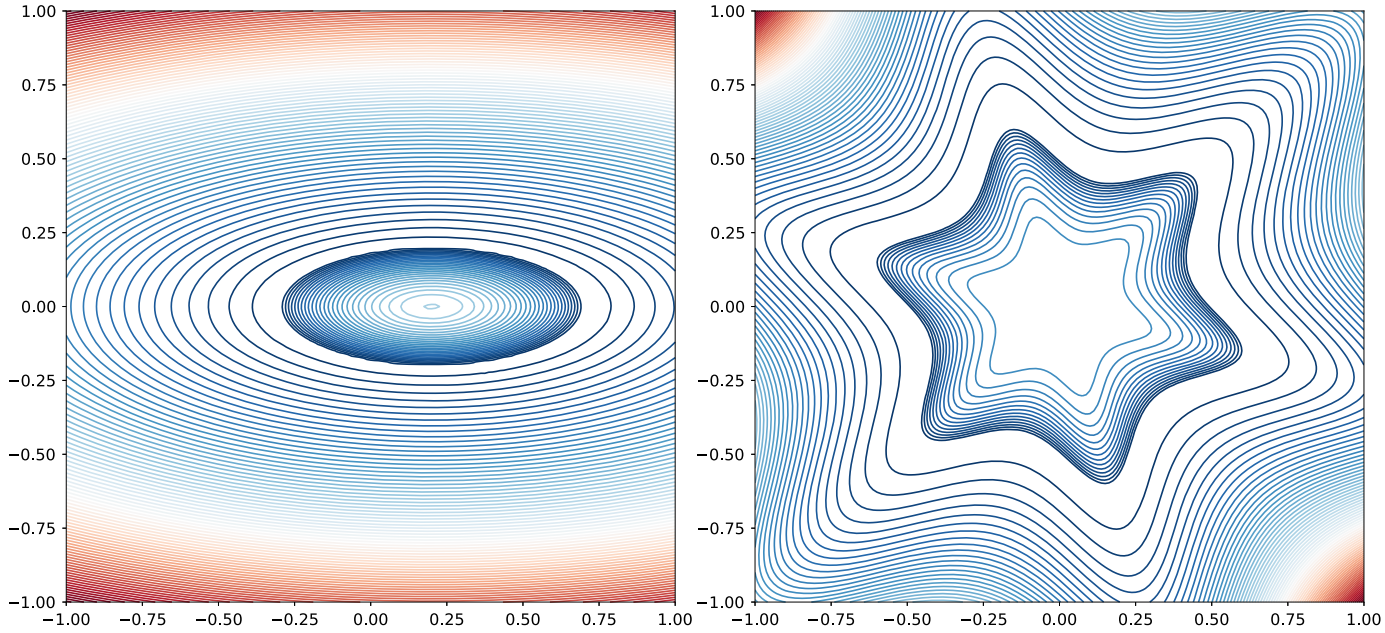

Fig. 6. Contour plots for numerical solution of Example 1 (Left) and Example 2 (Right) when $N = 160$.

Table 3
Errors of IFE solution u_h^1 in Example 2 at the ending time $t = 1$.

N	$\|u_h^1 - u^1\|_{L^\infty}$	order	$\|u_h^1 - u^1\|_{L^2}$	order	$\|u_h^1 - u^1\|_{H^1}$	order
10	1.3511×10^{-2}		1.0666×10^{-2}		1.4207×10^{-1}	
20	9.5144×10^{-3}	0.51	2.8976×10^{-3}	1.88	8.7907×10^{-2}	0.69
40	4.6819×10^{-3}	1.02	6.5421×10^{-4}	2.15	4.1211×10^{-2}	1.09
80	9.0997×10^{-4}	2.36	1.4037×10^{-4}	2.22	1.6755×10^{-2}	1.30
160	3.5321×10^{-4}	1.37	3.5395×10^{-5}	1.99	7.9007×10^{-3}	1.08
320	1.0016×10^{-4}	1.82	8.2650×10^{-6}	2.10	3.8282×10^{-3}	1.05
640	1.8367×10^{-5}	2.45	1.9017×10^{-6}	2.12	1.8453×10^{-3}	1.05

Table 4
Errors of IFE solution u_h^2 in Example 2 at the ending time $t = 1$.

N	$\|u_h^2 - u^2\|_{L^\infty}$	order	$\|u_h^2 - u^2\|_{L^2}$	order	$\|u_h^2 - u^2\|_{H^1}$	order
10	1.3511×10^{-2}		1.0666×10^{-2}		1.4207×10^{-1}	
20	9.5144×10^{-3}	0.51	2.8976×10^{-3}	1.88	8.7907×10^{-2}	0.69
40	4.6819×10^{-3}	1.02	6.5421×10^{-4}	2.15	4.1211×10^{-2}	1.09
80	9.0997×10^{-4}	2.36	1.4037×10^{-4}	2.22	1.6755×10^{-2}	1.30
160	3.5321×10^{-4}	1.37	3.5395×10^{-5}	1.99	7.9007×10^{-3}	1.08
320	1.0016×10^{-4}	1.82	8.2650×10^{-6}	2.10	3.8282×10^{-3}	1.05
640	1.8367×10^{-5}	2.45	1.9017×10^{-6}	2.12	1.8453×10^{-3}	1.05

and u_h^2 are almost independent with time L, in a steady and nearly periodic type of propagation mode. We emphasize that this example shows the advantage of our method for long time simulation. The related sharper theoretical results with respect to time L are left for future investigation.

Example 4 *(A traveling wave problem)*. In this example, we consider a traveling wave problem inspired by numerical examples in [1]. A circular interface $\Gamma = \{(x, y) \in \Omega : x^2 + y^2 = r_0^2\}$ with $r_0 = 1/2$ is considered in this example. For simplicity, we set the external force $\mathbf{f} = \mathbf{0}$ and initial conditions to be:

$$\begin{aligned} \boldsymbol{\omega}_0(x, y) &= \begin{pmatrix} -(200 + \frac{1000x}{3}) \exp[-200(1 + \frac{5x}{3})^2] \\ 0 \end{pmatrix}, \\ \boldsymbol{\omega}_1(x, y) &= \begin{pmatrix} [-72 + \frac{400000}{3}(1 + \frac{5x}{3})^2] \exp[-200(1 + \frac{5x}{3})^2] \\ 0 \end{pmatrix}, \end{aligned} \tag{5.4}$$

with periodic boundary condition. The solution of this problem describes the traveling of a band-shape plane wave from left to right along x-axis. The Lamé parameters are chosen to be $\lambda^+ = 1.0$, $\mu^+ = 0.01$, $\lambda^- = 0.1$, $\mu^- = 0.1$.

In our test, we slightly modify the stiffness matrix $\mathbf{K}$ to accommodate the periodic boundary condition while preserving the symmetric positive definiteness introduced in [6]. The heat plots of displacement $\mathbf{u}$ at time points $t = 0$, 0.105, 0.25, and 0.4 are shown in Fig. 8. In our tests, we set the spatial mesh size $N = 400$ and $\tau = 5 \times 10^{-4}$. Since it is difficult to obtain the exact solution for this example, we compare the cross sections of

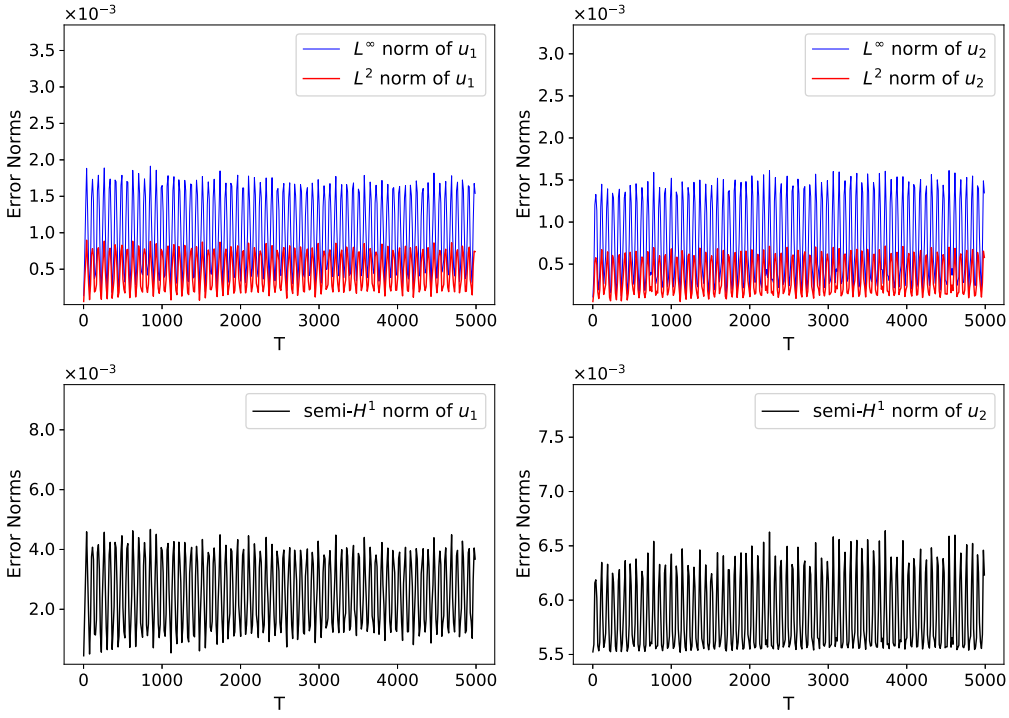

Fig. 7. Error Norms of Example 3 with respect to time when $N = 40$, $\tau = 1/320$.

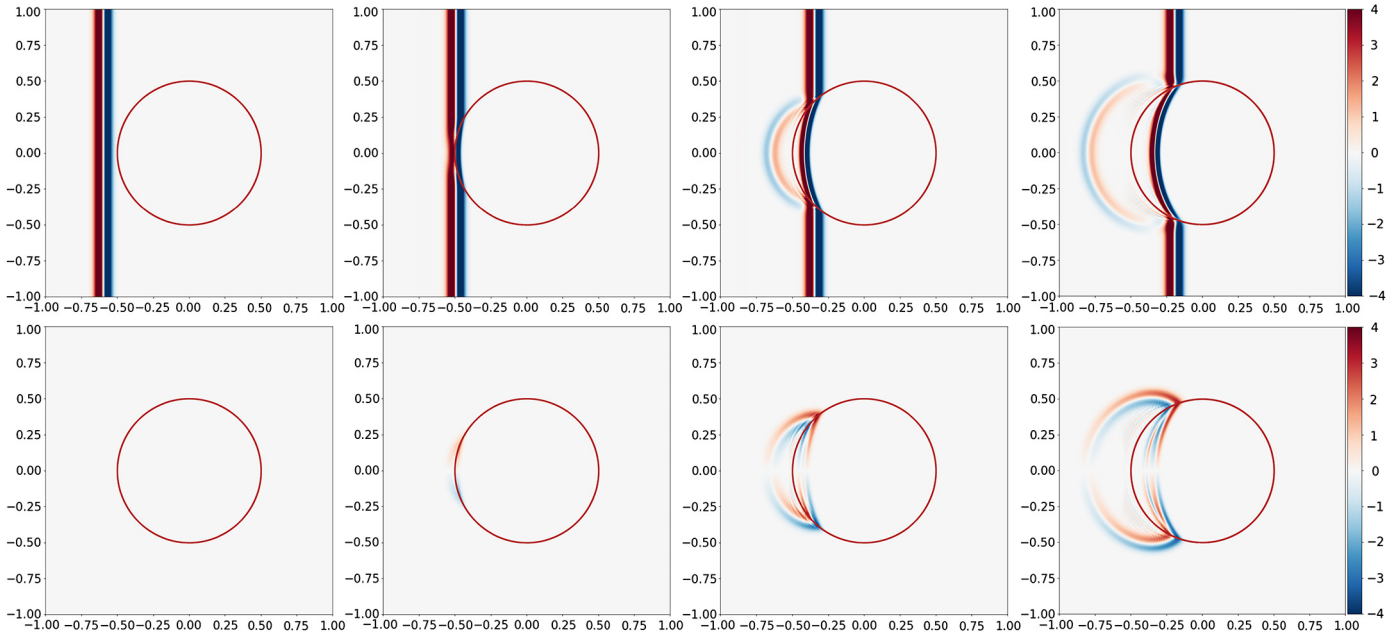

Fig. 8. First row: heat plots of u_1 at time point $T = 0, 0.105, 0.25, 0.4$ when $N = 400$. Second row: heat plots of u_2 at time point $T = 0, 0.105, 0.25, 0.4$.

numerical solutions at $y = 0$ at $t = 0.24$ and $t = 0.4$ for the meshes $N = 300$ and $N = 400$, respectively. For these two mesh sizes, we choose same time step $\tau = 5 \times 10^{-4}$, and the comparison is shown in Fig. 9. The numerical results of two meshes are observed to match with each other very well, which indicates the convergence of our numerical solutions.

6. Conclusion

In this paper, we proposed semi discrete and fully discrete numerical schemes for elastodynamics interface problems. For spatial discretization, we used linear or bilinear immersed finite element spaces and the partially penalized scheme. We proved properties of these IFE space including the norm equivalence and inverse inequalities. For fully discrete scheme, we used a θ-scheme with $\theta = 1/4$. Both semi-discrete and fully discrete schemes were analyzed and proved to converge optimally in the energy, L^2 and semi-H^1 norms. Numerical experiments are provided to verify the theoretical results. In addition, the long time behavior has been considered to illustrate the stability of the scheme. We also demonstrated the applicability and performance of our method on the traveling wave problems.

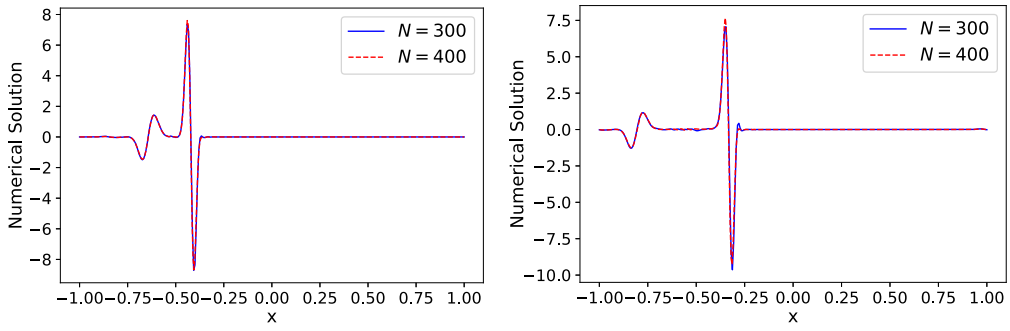

Fig. 9. Comparison of cross sections of u_1 numerical solution when $N = 300$ and $N = 400$, left: $T = 0.24$, right: $T = 0.4$.

Data availability

No data was used for the research described in the article.

Acknowledgements

The authors would like to thank Prof. Yulong Xing at The Ohio State University for valuable advices and discussions. Songming Hou is partially supported by the Walter Koss Professorship fund made available through Louisiana Board of Regents, United States. Xu Zhang is partially supported by National Science Foundation Grant DMS-2110833, the ORAU Ralph E. Powe Junior Faculty Enhancement Award.

References

[1] Slimane Adjerid, Tao Lin, Haroun Meghaichi, An immersed discontinuous Galerkin method for wave propagation in acoustic elastic media, J. Comput. Phys. 472 (2023) 111651.
[2] Slimane Adjerid, Tao Lin, Qiao Zhuang, Error estimates for an immersed finite element method for second order hyperbolic equations in inhomogeneous media, J. Sci. Comput. 84 (2) (2020) 35.
[3] Susanne C. Brenner, Poincaré-Friedrichs inequalities for piecewise H^1 functions, SIAM J. Numer. Anal. 41 (1) (2003) 306–324.
[4] Susanne C. Brenner, Korn's inequalities for piecewise H^1 vector fields, Math. Comput. 73 (247) (2004) 1067–1087.
[5] Susanne C. Brenner, L. Ridgway Scott, The Mathematical Theory of Finite Element Methods, third edition, Texts in Applied Mathematics, vol. 15, Springer, New York, 2008.
[6] Yong Cao, Yuchuan Chu, Xiaoshi Zhang, Xu Zhang, Immersed finite element methods for unbounded interface problems with periodic structures, J. Comput. Appl. Math. 307 (2016) 72–81.
[7] Yanzhen Chang, The adaptive immersed interface finite element method for elasticity interface problems, J. Comput. Math. 30 (6) (2012) 629–642.
[8] Yuan Chen, Xu Zhang, A P_2-P_1 partially penalized immersed finite element method for Stokes interface problems, Int. J. Numer. Anal. Model. 18 (1) (2021) 120–141.
[9] Eric T. Chung, Yalchin Efendiev, Shubin Fu, Generalized multiscale finite element method for elasticity equations, GEM Int. J. Geomath. 5 (2) (2014) 225–254.
[10] Bernardo Cockburn, Dominik Schötzau, Jing Wang, Discontinuous Galerkin methods for incompressible elastic materials, Comput. Methods Appl. Mech. Eng. 195 (25–28) (2006) 3184–3204.
[11] John Dolbow, Nicolas Moës, Ted Belytschko, An extended finite element method for modeling crack growth with frictional contact, Comput. Methods Appl. Mech. Eng. 190 (51–52) (2001) 6825–6846.
[12] Yan Gong, Bo Li, Zhilin Li, Immersed-interface finite-element methods for elliptic interface problems with nonhomogeneous jump conditions, SIAM J. Numer. Anal. 46 (1) (2007/08) 472–495.
[13] Quentin Grimal, Bazle A. Gama, Salah Naili, Alexandre Watzky, John W. Gillespie Jr., Finite element study of high-speed blunt impact on thorax: linear elastic considerations, Int. J. Impact Eng. 30 (6) (2004) 665–683.
[14] Quentin Grimal, Salah Naili, Alexandre Watzky, A study of transient elastic wave propagation in a bimaterial modeling the thorax, Int. J. Solids Struct. 39 (20) (2002) 5345–5369.
[15] Quentin Grimal, Salah Naili, Alexandre Watzky, Transient elastic wave propagation in a spherically symmetric bimaterial medium modeling the thorax, Int. J. Solids Struct. 39 (25) (2002) 6103–6120.
[16] Ruchi Guo, Tao Lin, A higher degree immersed finite element method based on a Cauchy extension for elliptic interface problems, SIAM J. Numer. Anal. 57 (4) (2019) 1545–1573.
[17] Ruchi Guo, Tao Lin, Yanping Lin, Approximation capabilities of immersed finite element spaces for elasticity interface problems, Numer. Methods Partial Differ. Equ. 35 (3) (2019) 1243–1268.
[18] Ruchi Guo, Tao Lin, Yanping Lin, Error estimates for a partially penalized immersed finite element method for elasticity interface problems, ESAIM Math. Model. Numer. Anal. 54 (1) (2020) 1–24.
[19] Ruchi Guo, Tao Lin, Qiao Zhuang, Improved error estimation for the partially penalized immersed finite element methods for elliptic interface problems, Int. J. Numer. Anal. Model. 16 (4) (2019) 575–589.
[20] Ruchi Guo, Yulong Xing, Optimal energy conserving local discontinuous Galerkin methods for elastodynamics: semi and fully discrete error analysis, J. Sci. Comput. 87 (1) (2021) 13.
[21] Ruchi Guo, Xu Zhang, Solving three-dimensional interface problems with immersed finite elements: a-priori error analysis, J. Comput. Phys. 441 (2021) 110445.
[22] Johnny Guzmán, Manuel A. Sánchez, Marcus Sarkis, A finite element method for high-contrast interface problems with error estimates independent of contrast, J. Sci. Comput. 73 (1) (2017) 330–365.
[23] Peter Hansbo, Mats G. Larson, Discontinuous Galerkin and the Crouzeix-Raviart element: application to elasticity, M2AN Math. Model. Numer. Anal. 37 (1) (2003) 63–72.
[24] Peter Hansbo, Mats G. Larson, Karl Larsson, Cut finite element methods for linear elasticity problems, in: Geometrically Unfitted Finite Element Methods and Applications, in: Lect. Notes Comput. Sci. Eng., vol. 121, Springer, Cham, 2017, pp. 25–63.
[25] Xiaoming He, Tao Lin, Yanping Lin, Approximation capability of a bilinear immersed finite element space, Numer. Methods Partial Differ. Equ. 24 (5) (2008) 1265–1300.
[26] Xiaoming He, Tao Lin, Yanping Lin, Immersed finite element methods for elliptic interface problems with non-homogeneous jump conditions, Int. J. Numer. Anal. Model. 8 (2) (2011) 284–301.
[27] Songming Hou, Zhilin Li, Liqun Wang, Wei Wang, A numerical method for solving elasticity equations with interfaces, Commun. Comput. Phys. 12 (2) (2012) 595–612.
[28] Gwanghyun Jo, Young Do Kwak, A reduced Crouzeix-Raviart immersed finite element method for elasticity problems with interfaces, Comput. Methods Appl. Math. 20 (3) (2020) 501–516.
[29] Derrick Jones, Xu Zhang, A class of nonconforming immersed finite element methods for Stokes interface problems, J. Comput. Appl. Math. 392 (2021) 113493.
[30] Derrick Jones, Xu Zhang, A conforming-nonconforming mixed immersed finite element method for unsteady Stokes equations with moving interfaces, Electron. Res. Arch. 29 (5) (2021) 3171–3191.
[31] Samir Karaa, Finite element θ-schemes for the acoustic wave equation, Adv. Appl. Math. Mech. 3 (2) (2011) 181–203.
[32] Tao Lin, Yanping Lin, Xu Zhang, Partially penalized immersed finite element methods for elliptic interface problems, SIAM J. Numer. Anal. 53 (2) (2015) 1121–1144.

[33] Tao Lin, Dongwoo Sheen, Xu Zhang, A locking-free immersed finite element method for planar elasticity interface problems, J. Comput. Phys. 247 (2013) 228–247.
[34] Tao Lin, Qing Yang, Xu Zhang, Partially penalized immersed finite element methods for parabolic interface problems, Numer. Methods Partial Differ. Equ. 31 (6) (2015) 1925–1947.
[35] Tao Lin, Xu Zhang, Linear and bilinear immersed finite elements for planar elasticity interface problems, J. Comput. Appl. Math. 236 (18) (2012) 4681–4699.
[36] Tao Lin, Qiao Zhuang, Optimal error bounds for partially penalized immersed finite element methods for parabolic interface problems, J. Comput. Appl. Math. 366 (2020) 112401.
[37] HuiPeng, Ruishu Wang, Xiuli Wang, Yongkui Zou, Weak Galerkin finite element method for linear elasticity interface problems, Appl. Math. Comput. 439 (2023) 127589.
[38] Fangfang Qin, Jinru Chen, Zhilin Li, Mingchao Cai, A Cartesian grid nonconforming immersed finite element method for planar elasticity interface problems, Comput. Math. Appl. 73 (3) (2017) 404–418.
[39] Fred Schwab, Robert Burridge, The interface problem in model seismology, Geophysics 33 (3) (1968) 473–480.
[40] Simon Sticko, Gustav Ludvigsson, Gunilla Kreiss, High-order cut finite elements for the elastic wave equation, Adv. Comput. Math. 46 (3) (2020) 45.
[41] S.K. Tomar, M.L. Gogna, Reflection and refraction of coupled transverse and micro-rotational waves at an interface between two different micropolar elastic media in welded contact, Int. J. Eng. Sci. 33 (4) (1995) 485–496.
[42] S.K. Tomar, M.L. Gogna, Reflection and refraction of longitudinal wave at an interface between two micropolar elastic solids in welded contact, J. Acoust. Soc. Am. 97 (2) (1995) 822–830.
[43] Chunmei Wang, Shangyou Zhang, A weak Galerkin method for elasticity interface problems, J. Comput. Appl. Math. 419 (2023) 114726.
[44] Jin Wang, Xu Zhang, Qiao Zhuang, An immersed Crouzeix-Raviart finite element method for Navier-Stokes equations with moving interfaces, Int. J. Numer. Anal. Model. 19 (4) (2022) 563–586.
[45] T. Warburton, J.S. Hesthaven, On the constants in hp-finite element trace inverse inequalities, Comput. Methods Appl. Mech. Eng. 192 (25) (2003) 2765–2773.
[46] Yuanming Xiao, Jinchao Xu, Fei Wang, High-order extended finite element methods for solving interface problems, Comput. Methods Appl. Mech. Eng. 364 (2020) 112964.
[47] Qing Yang, Numerical analysis of partially penalized immersed finite element methods for hyperbolic interface problems, Numer. Math. Theory Methods Appl. 11 (2) (2018) 272–298.
[48] Xingzhou Yang, Immersed interface method for elasticity problems with interfaces, PhD thesis, North Carolina State University, 2004.
[49] Qiao Zhuang, Ruchi Guo, High degree discontinuous Petrov-Galerkin immersed finite element methods using fictitious elements for elliptic interface problems, J. Comput. Appl. Math. 362 (2019) 560–573.
[50] O.C. Zienkiewicz, R.L. Taylor, The Finite Element Method, vol. 2, fifth edition, Butterworth-Heinemann, Oxford, 2000, Solid mechanics.